

₁ Physics-Infused Reduced-Order Modeling for Analysis of
₂ Ablating Hypersonic Thermal Protection Systems

₃

₄ November 22, 2025

₅

Abstract

This work presents a *physics-infused reduced-order modeling* (PIROM) framework towards design, analysis, and optimization of non-decomposing ablating hypersonic thermal protection systems (TPS), and is demonstrated via the modeling of transient thermo-ablative responses of multi-layered hypersonic TPS. The PIROM architecture integrates a reduced-physics backbone, based on the lumped-capacitance model (LCM) and a surface recession model (SRM), with data-driven correction dynamics formulated via a coarse-graining approach rooted in the Mori-Zwanzig formalism. The LCM is coupled to the SRM to capture the one-dimensional surface recession of the ablating TPS as a function of the surface temperature. While the LCM and SRM capture the dominant physics of the ablating TPS response, the correction terms compensate for residual dynamics arising from higher-order non-linear interactions and temperature-advection effects due to surface recession. The PIROM consistently achieves errors of $\approx 0.5\%$ for a wide range of extrapolative settings of design parameters involving time-and-space varying boundary conditions and SRM models, and improves by an order of magnitude by the LCM alone. Moreover, the PIROM delivers online evaluations that are two orders of magnitude faster than the full-order model (FOM). These results demonstrate that PIROM effectively reconciles the trade-offs between accuracy, generalizability, and efficiency, providing a promising framework for optimizing multi-physical dynamical systems, such as TPS, under diverse operating conditions.

₂₅

1 Introduction

₂₆ At hypersonic speeds, aerospace vehicles experience extreme aero-thermo-dynamic environments that require specialized thermal protection systems (TPS) to shield internal sub-
₂₇ structures, electronics, and possibly crew members from the intense aerodynamic heating.
₂₈ The TPS is often composed of ablating materials – a high-temperature capable fibrous material injected with a resin that fills the pore network and strengthens the composite [1]. The
₂₉ TPS design promotes the exchange of mass through thermal and chemical reactions (i.e.,
₃₀ ablation), effectively mitigating heat transfer to the sub-structures. As a result, accurate
₃₁ prediction for the ablating TPS response under extreme hypersonic heating becomes criti-
₃₂ cal to ensuring survivability, performance, and safety of hypersonic vehicles. Not only is it
₃₃ necessary to assess the performance of the thermal management systems, but also the shape
₃₄ of the vehicle.
₃₅

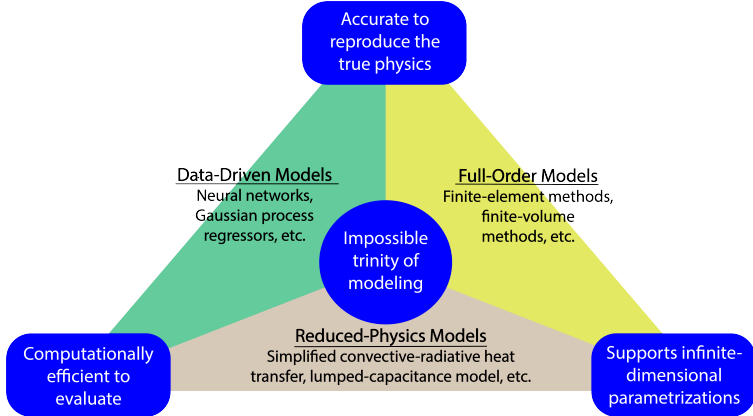


Figure 1: The impossible trinity of modeling: accuracy, generalizability, and efficiency.

36 changes of the vehicle’s outer surface induced by the ablating material, and its impact on
37 the aerodynamics, structural integrity, and controllability.

38 Even with today’s advancements in computational resources and numerical methods,
39 high-fidelity simulations of ablating TPS remains a formidable challenge, both theoretically
40 and computationally. On the theoretical side, the thermo-chemical reactions, coupled with
41 the irregular pore network structure and ablating boundaries, translate into complex non-
42 linear equations governing multi-physical interactions across several spatio-temporal scales [1,
43 8]. On the computational side, numerical approaches based on finite-element methods (FEM)
44 yield semi-discrete systems of differential equations modeling the transient thermo-ablative
45 response of the TPS [5]. The FEM discretizations lead to high-dimensional systems of
46 equations, resulting in prohibitive computational costs for many-query applications such as
47 design, optimization, uncertainty quantification, and real-time applications, where possibly
48 thousands of model evaluations are required.

49 Reduced-order models (ROMs) have emerged as a promising approach to alleviate the
50 computational costs of high-fidelity simulations [6, 11]. Ideally, a ROM should be: (1) ac-
51 curate to reproduce high-fidelity solutions, (2) support continuous or infinite-dimensional
52 design parameters such as geometrical shapes and material distributions, (3) be computa-
53 tional efficient to evaluate to allow for fast turnaround times in design optimization. However,
54 the above three capabilities usually form an *impossible trinity of modeling*, as illustrated in
55 Fig. 1; building a ROM that achieves any two capabilities sacrifices the third.

56 The impossible trinity poses a significant challenge in the development fo ROMs for the
57 multi-disciplinary transient analysis and optimization of ablating TPS. Specifically, full-order
58 models (FOMs), such as FEMs, offer high accuracy and robust generealization over design
59 spaces, but are computationally expensive to evaluate. Reduced-physics models (RPMs) –
60 such as simplified convective-radiative heat transfer or engineering correlations – achieve effi-
61 ciency adn broad applicability by ignoring certain non-linear or small-scale effects. However,
62 RPMs sacrifice accuracy for complex thermo-ablative responses, and it is generally not clear
63 how to leverage existing high-fidelity data to improve RPMs systematically [17].

64 with multi-physics couplings across a wide range of spatial and temporal scales [1, 8]. On
65 simplifying assumptions to reduce non-linearities, and make the resulting equations more
66 amenable for engineering application and design analysis [1]. For

67 Unfortunately, high-fidelity simulations of ablating TPS remains a formidable challenge
68 both theoretically and computationally.

69 On the theoretical side, the thermo-chemical reactions, coupled with the irregular pore
70 network structure, translate into simplifying assumptions to reduce non-linearities, and make
71 the resulting equations more amenable for engineering application and design analysis **x**.
72 For instance, one of the most notable codes is the one-dimensional **CMA** code that was
73 developed by Aerotherm Corporation in the 1960s **Howard2015**. Despite its practical use
74 in...

75 Another example is the CHarring Ablator Response (CHAR) ablation code, which ignores
76 elemental decompositions of the pyrolyzing gases, assumes the gases to be a mixture of perfect
77 gases in thermal equilibrium, and assumes no reaction or condensation with the porous
78 network [1].

79 In sum, the objectives of this work are as follows:

- 80 1. Extend the previous PIROM formulation in Ref. [16] to model transient thermo-
81 ablative response of multi-layered hypersonic TPS through a systematic coarse-graining
82 procedure based on the Mori-Zwanzig formalism.
- 83 2. Benchmark the accuracy, generalizability, and computational accelerations of the PIROM
84 against the RPM and the high-fidelity FEM solutions of ablating TPS, thus assessing
85 the PIROM's capabilities to solve the ITM in complex multi-physical non-linear dy-
86 namical systems.

87 2 Modeling of Ablating Thermal Protection Systems

88 This section presents the problem of modeling a non-decomposing ablating TPS subjected to
89 extreme hypersonic heating. Two different but mathematically connected solution strategies
90 are provided: (1) a high-fidelity full-order model (FOM) based on a finite element method
91 (FEM), and (2) a low-fidelity reduced-physics model (RPM) based on a lumped capacitance
92 model (LCM) and a one-dimensional surface velocity model (SRM). The FOM is compu-
93 tationally expensive but provides the highest fidelity, while the RPM is computationally
94 efficient but has low predictive fidelity; both models are amenable to high-dimensional de-
95 sign variables. The RPM is used in the subsequent sections for deriving the PIROM.

96 2.1 Governing Equations

97 The multi-physics for a non-decomposing ablating TPS involves the *energy equation* which
98 models the transient heat conduction inside the TPS, and the *pseudo-elasticity equation*,
99 which models the mesh motion due to surface recession. The governing PDEs for the ablating
100 TPS are summarized in this section.

101 2.1.1 Energy Equation

102 Consider a generic domain $\Omega \subset \mathbb{R}^d$, $d = 2$ or 3 , illustrated in Fig. 2. Let $\partial\Omega = \Gamma_q \cup \Gamma_T$ and
103 $\Gamma_q \cap \Gamma_T = \emptyset$, where a Neumann $q_b(x, t)$ boundary condition is prescribed on the Γ_q boundary,

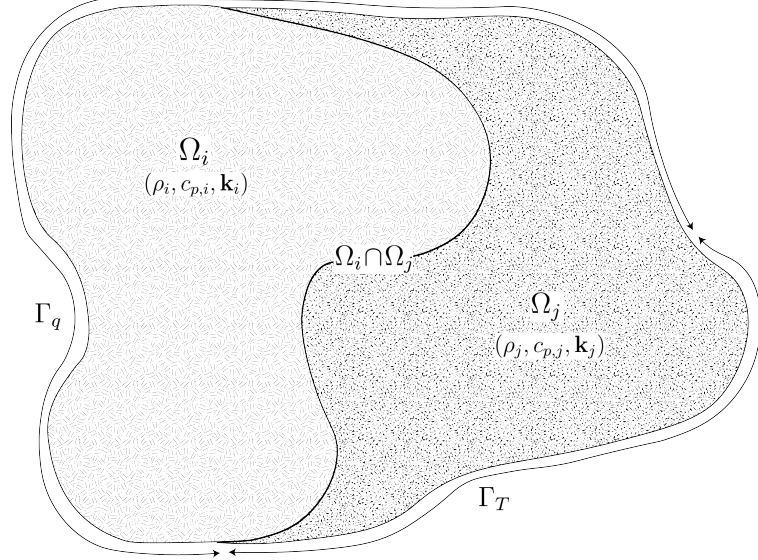


Figure 2: General domain Ω with prescribed Neumann and Dirichlet boundary conditions on Γ_q and Γ_T . Mesh displacement $w(x, t)$ occurs on the Γ_q boundary.

and represents the surface exposed to the hypersonic boundary layer. The Dirichlet $T_b(x, t)$ boundary condition is prescribed on the boundary Γ_T . The TPS is divided into N non-overlapping components $\{\Omega_i\}_{i=1}^N$, as illustrated in Fig. 2 for $N = 2$. The i -th component Ω_i is associated with material properties $(\rho_i, c_{p,i}, \mathbf{k}_i)$, that are assumed to be continuous within one component, and can be discontinuous across two neighboring components.

The transient heat conduction is described by the energy equation,

$$\rho c_p \left(\frac{\partial T}{\partial t} + \tilde{\mathbf{v}}(x, t) \cdot \nabla T \right) - \nabla \cdot (\mathbf{k} \nabla T) = 0, \quad x \in \Omega \quad (1a)$$

$$-\mathbf{k} \nabla T \cdot \mathbf{n} = q_b(x, t), \quad x \in \Gamma_q \quad (1b)$$

$$T(x, t) = T_b(x, t), \quad x \in \Gamma_T \quad (1c)$$

$$T(x, 0) = T_0(x), \quad x \in \Omega \quad (1d)$$

where the density ρ is constant, while the heat capacity c_p and thermal conductivity $\mathbf{k} \in \mathbb{R}^{d \times d}$ may depend on temperature. In the order they appear, the terms in eq. (1a) include, the unsteady energy storage, heat conduction, temperature advection due to mesh motion, and source terms due to boundary conditions. The boundary conditions for the energy equation includes Neumann eq. (1b) and Dirichlet eq. (1c) on Γ_T .

An Arbitrary Lagrangian-Eulerian (ALE) description is used to account for mesh motion due to surface recession, where $\tilde{\mathbf{v}}(x, t)$ is the relative velocity of the material with respect to the mesh,

$$\tilde{\mathbf{v}}(x, t) = \mathbf{v}_s(x, t) - \mathbf{v}_m(x, t) \quad (2)$$

where $\mathbf{v}_s(x, t)$ and $\mathbf{v}_m(x, t)$ are the physical material velocity and mesh velocity, respectively. In this work, the physical material velocity is assumed to be zero, i.e., $\mathbf{v}_s(x, t) = \mathbf{0}$, and thus the relative velocity is simply the negative of the mesh velocity, $\tilde{\mathbf{v}}(x, t) = -\mathbf{v}_m(x, t)$.

121 **2.1.2 Pseudo-Elasticity Equation**

122 The mesh motion is described by the steady-state pseudo-elasticity equation without body
123 forces,

$$\nabla \cdot \boldsymbol{\sigma}(\mathbf{w}) = \mathbf{0}, \quad \forall t \in \mathcal{T}, \mathbf{x} \in \Omega \quad (3a)$$

$$\mathbf{w}(\mathbf{x}, t) = \mathbf{w}_q(\mathbf{x}, t), \quad \forall t \in \mathcal{T}, \mathbf{x} \in \Gamma_q \quad (3b)$$

$$\mathbf{w}(\mathbf{x}, t) = \mathbf{0}, \quad \forall t \in \mathcal{T}, \mathbf{x} \notin \Gamma_q \quad (3c)$$

$$\mathbf{w}(\mathbf{x}, 0) = \mathbf{0}, \quad \forall \mathbf{x} \in \Omega \quad (3d)$$

124 where the stress tensor $\boldsymbol{\sigma}$ is related to the strain tensor $\boldsymbol{\epsilon}(\mathbf{w})$ through Hooke's law,

$$\boldsymbol{\sigma}(\mathbf{w}) = \mathbb{D} : \boldsymbol{\epsilon}(\mathbf{w})$$

125 where \mathbb{D} is the fourth-order positive definite elasticity tensor, and ":" is the double con-
126 traction of the full-order tensor \mathbb{D} with the second-order tensor $\boldsymbol{\epsilon}$. The elasticity tensor
127 ordinarily possess a number of symmetries, effectively reducing the number of components
128 that describe it [2]. The symmetric strain tensor $\boldsymbol{\epsilon}$ measures the deformation of the mesh
129 due to displacements $\mathbf{w}(x, t)$, and is defined as,

$$\boldsymbol{\epsilon}(\mathbf{w}) = \frac{1}{2} (\nabla \mathbf{w} + \nabla \mathbf{w}^\top)$$

130 The "material" properties for the mesh are chosen to tailor the mesh deformation, and need
131 not represent the actual material being modeled [1].

132 For the pseudo-elasticity equations, the boundary conditions include prescribed displace-
133 ments $\mathbf{w}_q(x, t)$ on the heated boundary Γ_q in eq. (3b), and zero displacements on the unheated
134 boundaries in eq. (3c). The initial condition for the mesh displacements is zero in eq. (3d).
135 Particularly, the surface velocity due to the ablating material is a function of the surface
136 temperature $T_q(x, t)$ for $x \in \Gamma_q$ on the heated boundary. For the i -th material component,
137 the mesh velocity on the heated boundary is imposed based on the following relation,

$$\hat{\mathbf{n}} \cdot \mathbf{v}_m(x, t) = f(T_q(x, t)), \quad x \in \Gamma_q \quad (4)$$

138 where $\hat{\mathbf{n}}$ is the unit normal vector on the heated boundary Γ_q , and f is a function obtained
139 from tabulated data for the material, commonly referred to as a B' table [1]. The B' table
140 provides a model for the recession velocity as a function of the surface temperature, and is
141 pre-computed based on high-fidelity simulations of the ablation process for a one-dimensional
142 slab of the material, and is independent of the TPS geometry. Provided the surface velocity,
143 the boundary condition in eq. (5) for the mesh displacements are computed by integrating
144 the surface velocity over time,

$$\mathbf{w}_q(x, t) = \int_0^t \mathbf{v}_m(x, \tau) d\tau \quad (5)$$

145 2.2 Full-Order Model: Finite-Element Method

146 To obtain the full-order numerical solution, the *energy equation* is spatially discretized using
 147 variational principles of the Discontinuous Galerkin (DG) method [5]. Note that the choice
 148 of DG approach is mainly for theoretical convenience, and is exclusively performed on the
 149 energy equation, as it is the surface temperature that drives the ablation process. The
 150 equivalence between DG and FEM is noted upon their convergence. For the *pseudo-elasticity*
 151 *equation* standard FEM is used to compute the mesh displacements based on the surface
 152 temperature provided by the DG solution of the energy equation [2].

153 Consider a conforming mesh partition domain, where each element belongs to one and
 154 only one component. Denote the collection of all M elements as $\{E_i\}_{i=1}^M$. In an element E_i ,
 155 its shared boundaries with another element E_j , Neumann BC, and Dirichlet BC are denoted
 156 as e_{ij} , e_{iq} , and e_{iT} , respectively. Lastly, $|e|$ denotes the length ($n_d = 2$) or area ($n_d = 3$) of a
 157 component boundary e .

158 For the i -th element, use a set of P trial functions, such as polynomials, to represent the
 159 temperature distribution,

$$T_i(x, t) = \sum_{l=1}^P \phi_l^i(x) u_l^i(t) \equiv \boldsymbol{\phi}_i^\top(x) \mathbf{u}_i(t), \quad i = 1, 2, \dots, M \quad (6)$$

160 Without loss of generality, the trial functions are assumed to be orthogonal, so that,

$$\int_{E_i} \phi_l^i(x) \phi_k^i(x) d\Omega = 0, \quad l \neq k$$

161 where δ_{lk} is the Kronecker delta function. Furthermore, for simplicity, choose $\phi_1^i = 1$. Thus,
 162 by orthogonality,

$$\int_{E_i} \phi_1^i(x) d\Omega = |E_i|, \quad \int_{E_i} \phi_k^i(x) d\Omega = 0, \quad k = 2, 3, \dots, P$$

163 Under the choice of basis functions, u_1^i is simply the average temperature of element E_i ,
 164 denoted as \bar{u}_i .

165 By standard variational processes, e.g., [5], the element-wise governing equation is de-
 166 noted as,

$$\mathbf{A}_i \dot{\mathbf{u}}_i = (\mathbf{B}_i + \mathbf{C}_i) \mathbf{u}_i + \sum_{j \in \mathcal{N}_i \cup \{T_b\}} (\mathbf{B}_{ij}^i \mathbf{u}_i + \mathbf{B}_{ij}^j \mathbf{u}_j) + \mathbf{f}_i(t), \quad \text{for } i = 1, 2, \dots, M \quad (7)$$

167 which is collected as the following ODE for the all the elements in the mesh,

$$\mathbf{A}(\mathbf{u}) \dot{\mathbf{u}} = [\mathbf{B}(\mathbf{u}) + \mathbf{C}(\mathbf{u})] \mathbf{u} + \mathbf{f}(t) \quad (8)$$

168 where $\mathbf{u} = [\mathbf{u}_1, \mathbf{u}_2, \dots, \mathbf{u}_M]^\top \in \mathbb{R}^{MP}$ includes all the DG variables, $\mathbf{f} \in \mathbb{R}^{MP}$ is the exter-
 169 nal forcing, and the system matrices \mathbf{A} , \mathbf{B} , and \mathbf{C} are the matrices due to heat capacity,
 170 heat conduction, and temperature advection due to mesh motion, respectively. A detailed

¹⁷¹ derivation of eqs. (7) and (8) and their matrices is provided in Appendix A.

¹⁷² 2.3 Reduced-Physics Model

¹⁷³ The RPM for predicting the response of the ablating TPS consists of two components: (1) the
¹⁷⁴ *lumped-capacitance model* (LCM), and (2) the *surface recession model* (SRM). The LCM is
¹⁷⁵ described as a first-order system of ODEs for predicting the average temperatures inside the
¹⁷⁶ components of the TPS, and provides a low-fidelity (under estimate) for the component's
¹⁷⁷ surface temperature. The SRM provides a relation between the surface temperature and
¹⁷⁸ the surface recession velocity based on pre-computed B' tables for the material, enabling the
¹⁷⁹ computation of one-dimensional surface displacements. The LCM and SRM are combined to
¹⁸⁰ define the RPM, providing low-fidelity estimates for the temperatures and surface recession
¹⁸¹ of the ablating TPS.

¹⁸² 2.3.1 Lumped Capacitance Model

¹⁸³ A general form of the LCM is provided in this section; details regarding the derivation
¹⁸⁴ for the four-component TPS used in the results section are provided in Appendix A. The
¹⁸⁵ LCM is a classical physics-based low-order model for predicting the temporal variation of
¹⁸⁶ average temperature in multiple interconnected components [9]. The LCM is derived at the
¹⁸⁷ component level from a point of view of energy conservation, and leads to the following
¹⁸⁸ system of ODEs for the average temperatures on the components,

$$\bar{\mathbf{A}}\dot{\bar{\mathbf{u}}} = \bar{\mathbf{B}}\bar{\mathbf{u}} + \bar{\mathbf{f}}(t) \quad (9)$$

¹⁸⁹ Where the states and inputs,

$$\bar{\mathbf{u}} = [\bar{u}_1, \bar{u}_2, \dots, \bar{u}_N]^\top \in \mathbb{R}^N, \quad \bar{\mathbf{f}} = [\bar{f}_1, \bar{f}_2, \dots, \bar{f}_N]^\top \in \mathbb{R}^N \quad (10)$$

¹⁹⁰ include the average temperatures $\bar{\mathbf{u}}$ and spatially-integrated inputs $\bar{\mathbf{f}}$ for the N components.

¹⁹¹ For $i, j = 1, 2, \dots, N$ the (i, j) -th elements of the $\bar{\mathbf{A}} \in \mathbb{R}^{N \times N}$, $\bar{\mathbf{B}} \in \mathbb{R}^{N \times N}$, and $\bar{\mathbf{f}} \in \mathbb{R}^N$
¹⁹² matrices are given by,

$$\bar{A}_i = \begin{cases} \int_{\Omega_i} \rho c_p d\Omega_i, & i = j \\ 0, & i \neq j \end{cases}, \quad \bar{B}_{ij} = \begin{cases} \sum_{j \in \mathcal{N}_i \cup \{T_b\}} \bar{B}_{ij}^i, & i = j \\ \bar{B}_{ij}^{(j)}, & i \neq j \end{cases}, \quad (11a)$$

$$\mathbf{f}_i = \begin{cases} |e_{iq}| \bar{q}_i + \frac{|e_{iT}|}{R_i} \bar{T}_i, & i = j \\ 0, & i \neq j \end{cases} \quad (11b)$$

¹⁹³ where,

$$\bar{q}_i = \frac{1}{|e_{iq}|} \int_{e_{iq}} q_b d e_{iq}, \quad \bar{T}_i = \frac{1}{|e_{iT}|} \int_{e_{iT}} T_b d e_{iT}, \quad \bar{B}_{ij}^i = -\frac{|e_{ij}|}{R_{ij}}, \quad \bar{B}_{ij}^j = \frac{|e_{ij}|}{R_{ij}} \quad (12)$$

¹⁹⁴ where R_{ij} is the equivalent thermal resistance between two neighboring components Ω_i and
¹⁹⁵ Ω_j , and R_i is the thermal resistance between component Ω_i and the Dirichlet boundary.

¹⁹⁶ The thermal resistances are computed based on the geometry and material properties of the
¹⁹⁷ components; details regarding their computation are provided in Appendix A.

¹⁹⁸ 2.3.2 Surface Recession Model

¹⁹⁹ The displacement is assumed to be *one-dimensional* on the heated boundary Γ_q , i.e., the
²⁰⁰ surface recedes only in the direction of the applied load. Displacements perpendicular to
²⁰¹ the direction of the applied load are assumed small and are neglected. Thus, for the i -th
²⁰² ablating component, the one-dimensional SRM considered in this work takes the form,

$$\dot{\mathbf{w}} = \boldsymbol{\Xi} \bar{\mathbf{u}} - \tilde{\mathbf{f}} \quad (13)$$

²⁰³ where $\boldsymbol{\Xi} = \text{diag}(\alpha_1, \dots, \alpha_{\tilde{N}})$ and $\tilde{\mathbf{f}} = (\alpha_1 \bar{u}_{0,1}, \dots, \alpha_{\tilde{N}} \bar{u}_{0,\tilde{N}})^\top$. The constants α_i are small
²⁰⁴ material-dependent constants, determined from the B' table, and $\bar{u}_{0,i}$ is the constant initial
²⁰⁵ temperature of the ablative component. The SRM provides a relation between the surface's
²⁰⁶ temperature and recession velocity, based on pre-computed B' tables for the material.

²⁰⁷ 2.3.3 Thermo-Ablative Reduced-Physics Model

²⁰⁸ The LCM and SRM are combined to define the RPM for predicting the thermo-ablative
²⁰⁹ response of the TPS under hypersonic boundary layers. Specifically, the RPM is defined as
²¹⁰ the LCM as in eq. (9), where the *geometry- and temperature-dependent matrices* $\tilde{\mathbf{A}}$, $\tilde{\mathbf{B}}$, and
²¹¹ $\tilde{\mathbf{f}}$ are updated at each time step based on the current temperature $\bar{\mathbf{u}}$ and displacements \mathbf{w}
²¹² provided by the SRM. The RPM is formally stated as,

$$\tilde{\mathbf{A}}(\mathbf{s})\dot{\mathbf{s}} = \tilde{\mathbf{B}}(\mathbf{s})\mathbf{s} + \tilde{\mathbf{F}}(t) \quad (14a)$$

$$\tilde{\mathbf{z}} = \mathbf{I}\mathbf{s} \quad (14b)$$

²¹³ where the state $\mathbf{s} = [\bar{\mathbf{u}}, \mathbf{w}]^\top \in \mathbb{R}^{N+\tilde{N}}$ includes the *average temperature* and *one-dimensional*
²¹⁴ *surface displacements*, and \tilde{N} is the number of ablating components with $\tilde{N} \leq N$. Moreover,
²¹⁵ the observables are defined as $\mathbf{z} = [\bar{\mathbf{u}}, \mathbf{w}]^\top \in \mathbb{R}^{N+\tilde{N}}$. The matrices are given as,

$$\tilde{\mathbf{A}}(\mathbf{s}) = \begin{bmatrix} \bar{\mathbf{A}}(\mathbf{s}) & \mathbf{0} \\ \mathbf{0} & \mathbf{I} \end{bmatrix}, \quad \tilde{\mathbf{B}}(\mathbf{s}) = \begin{bmatrix} \bar{\mathbf{B}}(\mathbf{s}) & \mathbf{0} \\ \boldsymbol{\Xi} & \mathbf{0} \end{bmatrix}, \quad \tilde{\mathbf{F}}(t) = \begin{bmatrix} \bar{\mathbf{f}}(t) \\ -\tilde{\mathbf{f}} \end{bmatrix} \quad (15)$$

²¹⁶ In the matrices $\tilde{\mathbf{A}}$ and $\tilde{\mathbf{B}}$, the surface displacements \mathbf{w} are used to define the dimensions for
²¹⁷ the Ω_i component used in eqs. (11) and (12), thus effectively coupling the LCM and SRM.

²¹⁸ 2.4 Summary of Modeling Approaches

²¹⁹ The FOM (i.e., FEM) and RPM (i.e., LCM with SRM) are two different but mathemati-
²²⁰ cally connected solution strategies. Particularly, the LCM in eq. (9) not only resembles the
²²¹ functional form of the DG model in eq. (8), but can be viewed as a special case of the latter,
²²² where the mesh partition is extremely coarse, and the trial and test functions are piece-wise
²²³ constants. This removes all spatial variations within each component, and neglects advection
²²⁴ effects due to mesh motion.

225 For example, consider the case where each component Ω_i is treated as one single element,
 226 and each element employs one constant basis function $\phi_i = 1$. The element-wise DG model
 227 in eq. (7) simplifies into a scalar ODE,

$$\mathbf{A}^{(i)} = \bar{A}_i, \quad \mathbf{C}^{(i)} = 0, \quad \mathbf{B}_{ij}^{(i)} = -\sigma|e_{ij}|, \quad \mathbf{B}_{ij}^{(j)} = \sigma|e_{ij}|, \quad \mathbf{f}_i = |e_{iq}|\bar{q}_i + \sigma|e_{iT}|\bar{T}_i \quad (16)$$

228 Clearly, the LCM is a coarse zeroth-order DG model with the inverse of thermal resistance
 229 chosen as the element-wise penalty factors. Or conversely, the DG model is a refined version
 230 of LCM via *hp*-adaptation.

231 The FOM and RPM represent two extremes in the modeling fidelity and computational
 232 cost spectrum. On one hand, the FOM is the most accurate but computationally expensive
 233 to evaluate due to the fine mesh discretizations for both the temperature and displacement
 234 fields, leading to possibly millions of state variables. On the other hand, the RPM consid-
 235 ers only the average temperature of the material, from which the one-dimensional surface
 236 displacements are computed by integrating eq. (13). This considerably reduces the com-
 237 putational cost, but sacrifices local temperature information that are critical to properly
 238 capture higher-order effects due to mesh motion and thermal gradients within each compo-
 239 nent. Thus, neither the FOM nor the RPM is an universal approach for real-world analysis,
 240 design, and optimization tasks for ablating TPS, where thousands of high-fidelity model
 241 evaluations may be necessary. This issue motivates the development of the PIROM, which
 242 can achieve the fidelity of FOM at a computational cost close to the RPM, while maintaining
 243 the generalizability to model parameters.

244 3 Physics-Infused Reduced-Order Modeling

245 The formulation of PIROM for ablating TPS starts by connecting the FOM, i.e., the DG-
 246 FEM, and the RPM, i.e., the LCM, via a coarse-graining procedure. This procedure pin-
 247 points the missing dynamics in the LCM when compared to DG-FEM. Subsequently, the
 248 Mori-Zwanzig (MZ) formalism is employed to determine the model form for the missing dy-
 249 namics in PIROM. Lastly, the data-driven identification of the missing dynamics in PIROM
 250 is presented.

251 3.1 Deriving the Reduced-Physics Model via Coarse-Graining

252 The subsequent coarse-graining formulation is performed on the DG-FEM in eq. (8) to derive
 253 the LCM in eq. (9). This process constraints the trial function space of a full-order DG model
 254 to a subset of piece-wise constants, so that the variables \mathbf{u} , matrices \mathbf{A} , \mathbf{B} , and \mathbf{C} , and forcing
 255 vector \mathbf{f} are all approximated using a single state associated to the average temperature.
 256 Note that the coarse-graining is exclusively performed on the thermal dynamics, as it is
 257 the surface temperature that drives the one-dimensional recession via the SRM. Hence, the
 258 coarse-graining of the mesh dynamics is not included in the following procedure.

259 **3.1.1 Coarse-Graining of States**

260 Consider a DG model as in eq. (8) for M elements and an LCM as in eq. (9) for N components;
 261 clearly $M \gg N$. Let $\mathcal{V}_j = \{i | E_i \in \Omega_j\}$ be the indices of the elements belonging to the j -th
 262 component, so $E_i \in \Omega_j$ for all $i \in \mathcal{V}_j$. The number of elements in the j -th component is $|\mathcal{V}_j|$.
 263 The average temperature on Ω_j is,

$$\bar{u}_j = \frac{1}{|\Omega_j|} \sum_{i \in \mathcal{V}_j} \int_{E^{(i)}} \boldsymbol{\phi}^{(i)}(x)^T \mathbf{u}^{(i)} d\Omega = \frac{1}{|\Omega_j|} \sum_{i \in \mathcal{V}_j} |E_i| \boldsymbol{\varphi}_i^{j\top} \mathbf{u}^{(i)}, \quad j = 1, 2, \dots, N \quad (17)$$

264 where $|\Omega_j|$ and $|E_i|$ denote the area ($d = 2$) or volume ($d = 3$) of component j and element
 265 i , respectively. The orthogonal basis functions are defined as $\boldsymbol{\varphi}_i^{j\top} = [1, 0, \dots, 0]^\top \in \mathbb{R}^P$.

266 Conversely, given the average temperatures of the N components, $\bar{\mathbf{u}}$, the states of an
 267 arbitrary element E_i is written as,

$$\mathbf{u}^{(i)} = \sum_{k=1}^N \boldsymbol{\varphi}_i^k \bar{u}_k + \delta \mathbf{u}^{(i)}, \quad i = 1, 2, \dots, M \quad (18)$$

268 where $\boldsymbol{\varphi}_i^k = 0$ if $i \notin \mathcal{V}_k$, and $\delta \mathbf{u}^{(i)}$ represents the deviation from the average temperature and
 269 satisfies the orthogonality condition $\boldsymbol{\varphi}_i^{k\top} \delta \mathbf{u}^{(i)} = 0$ for all k .

270 Equations eqs. (17) and (18) are combined and written in matrix form as,

$$\bar{\mathbf{u}} = \boldsymbol{\Phi}^+ \mathbf{u}, \quad \mathbf{u} = \boldsymbol{\Phi} \mathbf{u} + \delta \mathbf{u} \quad (19)$$

271 where $\boldsymbol{\Phi} \in \mathbb{R}^{MP \times N}$ is a matrix of $M \times N$ blocks, with the (i, j) -th block as $\boldsymbol{\varphi}_i^j$, $\boldsymbol{\Phi}^+ \in \mathbb{R}^{N \times MP}$
 272 is the left inverse of $\boldsymbol{\Phi}$, with the (i, j) -th block as $\boldsymbol{\varphi}_i^{j+} = \frac{|E_i|}{|\Omega_j|} \boldsymbol{\varphi}_i^{j\top}$, and $\delta \mathbf{u}$ is the collection of
 273 deviations. By their definitions, $\boldsymbol{\Phi}^+ \boldsymbol{\Phi} = \mathbf{I}$ and $\boldsymbol{\Phi}^+ \delta \mathbf{u} = \mathbf{0}$.

274 **3.1.2 Coarse-Graining of Dynamics**

275 The dependence of the matrices with respect to the displacements \mathbf{w} is dropped to isolate
 276 the analysis based on coarsened variables. Consider a function of states in the form of
 277 $\mathbf{M}(\mathbf{u})\mathbf{g}(\mathbf{u})$, where $\mathbf{g} : \mathbb{R}^{MP} \rightarrow \mathbb{R}^{MP}$ is a vector-valued function, and $\mathbf{M} : \mathbb{R}^{MP} \rightarrow \mathbb{R}^{p \times MP}$
 278 is a matrix-valued function with an arbitrary dimension p . Define the projection matrix
 279 $\mathbf{P} = \boldsymbol{\Phi} \boldsymbol{\Phi}^+$ and the projection operator \mathcal{P} as,

$$\begin{aligned} \mathcal{P} [\mathbf{M}(\mathbf{u})\mathbf{g}(\mathbf{u})] &= \mathbf{M}(\mathbf{P}\mathbf{u})\mathbf{g}(\mathbf{P}\mathbf{u}) \\ &= \mathbf{M}(\boldsymbol{\Phi}\bar{\mathbf{u}})\mathbf{g}(\boldsymbol{\Phi}\bar{\mathbf{u}}) \end{aligned} \quad (20)$$

280 so that the resulting function depends only on the average temperatures $\bar{\mathbf{u}}$. Correspondingly,
 281 the residual operator $\mathcal{Q} = \mathcal{I} - \mathcal{P}$, and $\mathcal{Q}[\mathbf{M}(\mathbf{u})\mathbf{g}(\mathbf{u})] = \mathbf{M}(\mathbf{u})\mathbf{g}(\mathbf{u}) - \mathbf{M}(\boldsymbol{\Phi}\bar{\mathbf{u}})\mathbf{g}(\boldsymbol{\Phi}\bar{\mathbf{u}})$. When
 282 the function is not separable, the projection operator is simply defined as $\mathcal{P}[\mathbf{g}(\mathbf{u})] = \mathbf{g}(\mathbf{P}\mathbf{u})$.

283 Subsequently, the operators defined above are applied to coarse-grain the dynamics. First,

²⁸⁴ write the DG-FEM in eq. (8) as,

$$\dot{\mathbf{u}} = \mathbf{A}(\mathbf{u})^{-1}\mathbf{B}(\mathbf{u})\mathbf{u} + \mathbf{A}(\mathbf{u})^{-1}\mathbf{C}(\mathbf{u})\mathbf{u} + \mathbf{A}(\mathbf{u})^{-1}\mathbf{f}(t) \quad (21)$$

²⁸⁵ and multiply both sides by Φ^+ to obtain,

$$\Phi^+\dot{\mathbf{u}} = \Phi^+(\Phi\dot{\mathbf{u}} + \delta\dot{\mathbf{u}}) = \dot{\bar{\mathbf{u}}} = \Phi^+\mathbf{r}(\mathbf{u}, t) \quad (22)$$

²⁸⁶ Apply the projection operator \mathcal{P} and the residual operator \mathcal{Q} to the right-hand side to obtain,

$$\dot{\bar{\mathbf{u}}} = \mathcal{P}[\Phi^+\mathbf{r}(\mathbf{u}, t)] + \mathcal{Q}[\Phi^+\mathbf{r}(\mathbf{u}, t)] \equiv \mathbf{r}^{(1)}(\mathbf{u}, t) + \mathbf{r}^{(2)}(\mathbf{u}, t) \quad (23)$$

²⁸⁷ where $\mathbf{r}^{(1)}(\mathbf{u}, t)$ is resolved dynamics that depends on $\bar{\mathbf{u}}$ only, and $\mathbf{r}^{(2)}(\mathbf{u}, t)$ is the un-resolved
²⁸⁸ or residual dynamics. Detailed derivations and analysis of $\mathbf{r}^{(1)}(\mathbf{u}, t)$ and $\mathbf{r}^{(2)}(\mathbf{u}, t)$ can be
²⁸⁹ found in the Appendix.

²⁹⁰ It follows from Ref. [16] that the resolved dynamics is exactly the LCM, where the
²⁹¹ advection term reduces to zero, i.e., $\bar{\mathbf{C}}(\bar{\mathbf{u}}) = \mathbf{0}$ as shown in the Appendix. Using the notation
²⁹² from eq. (9), it follows that,

$$\begin{aligned} \mathbf{r}^{(1)}(\mathbf{u}, t) &= \bar{\mathbf{A}}(\bar{\mathbf{u}})^{-1}\bar{\mathbf{B}}(\bar{\mathbf{u}})\bar{\mathbf{u}} + \bar{\mathbf{A}}(\bar{\mathbf{u}})^{-1}\bar{\mathbf{C}}(\bar{\mathbf{u}})\bar{\mathbf{u}} + \bar{\mathbf{A}}(\bar{\mathbf{u}})^{-1}\bar{\mathbf{f}}(\bar{\mathbf{u}}) \\ &= \bar{\mathbf{A}}(\bar{\mathbf{u}})^{-1}\bar{\mathbf{B}}(\bar{\mathbf{u}})\bar{\mathbf{u}} + \bar{\mathbf{A}}(\bar{\mathbf{u}})^{-1}\bar{\mathbf{f}}(t) \end{aligned} \quad (24)$$

²⁹³ where the following relations hold,

$$\bar{\mathbf{A}}(\bar{\mathbf{u}}) = \mathbf{W}(\Phi^+\mathbf{A}(\Phi\bar{\mathbf{u}})^{-1}\Phi)^{-1} \quad (25a)$$

$$\bar{\mathbf{B}}(\bar{\mathbf{u}}) = \mathbf{W}\Phi^+\mathbf{B}(\Phi\bar{\mathbf{u}})\Phi \quad (25b)$$

²⁹⁴ where $\mathbf{W} \in \mathbb{R}^{N \times N}$ is a diagonal matrix with the i -th element as $[\mathbf{W}]_{ii} = |\mathcal{V}_k|$ if $i \in \mathcal{V}_k$.
²⁹⁵ The examination of the second residual term $\mathbf{r}^{(2)}(\mathbf{u}, t)$ in eq. (23) is shown in the Appendix,
²⁹⁶ and demonstrates that the physical sources of missing dynamics in the LCM include: the
²⁹⁷ approximation of non-uniform temperature within each component as a constant, and the
²⁹⁸ elimination of the advection term due to coarse-graining. In sum, the above results not
²⁹⁹ only show that the LCM is a result of coarse-graining of the full-order DG-FEM, but also
³⁰⁰ reveal the discrepancies between the LCM and the DG-FEM. These discrepancies propagate
³⁰¹ into the SRM, which as a result of the averaging in the LCM formulation, under-predicts
³⁰² the surface recession rates. In the subsequent section, the discrepancies in the LCM are
³⁰³ corrected to formulate the PIROM.

³⁰⁴ 3.2 Physics-Infusion Via Mori-Zwanzig Formalism

³⁰⁵ The Mori-Zwanzig (MZ) formalism is an operator-projection technique used to derive ROMs
³⁰⁶ for high-dimensional dynamical systems, especially in statistical mechanics and fluid dy-
³⁰⁷ namics [13, 14, 15]. It provides an exact reformulation of a high-dimensional Markovian dy-
³⁰⁸ namical system, into a low-dimensional observable non-Markovian dynamical system. The
³⁰⁹ proposed ROM is subsequently developed based on the approximation to the non-Markovian
³¹⁰ term in the observable dynamics. Particularly, eq. (23) shows that the DG-FEM dynam-

311 ics can be decomposed into the resolved dynamics $\mathbf{r}^{(1)}(\mathbf{u}, t)$ and the orthogonal dynamics
312 $\mathbf{r}^{(2)}(\mathbf{u}, t)$, in the sense of $\mathcal{P}\mathbf{r}^{(2)} = 0$. In this case, the MZ formalism can be invoked to ex-
313 press the dynamics $\bar{\mathbf{u}}$ in terms of $\bar{\mathbf{u}}$ alone as the projected Generalized Langevin Equation
314 (GLE) [13, 14, 15],

$$\dot{\bar{\mathbf{u}}}(t) = \mathbf{r}^{(1)}(\bar{\mathbf{u}}, t) + \int_0^t \tilde{\kappa}(t, s, \bar{\mathbf{u}}) ds \quad (26)$$

315 where the first and second terms are referred to as the Markovian and non-Markovian terms,
316 respectively. The non-Markovian term accounts for the effects of past un-resolved states on
317 the current resolved states via a memory kernel $\tilde{\kappa}(t, s, \bar{\mathbf{u}})$, which in practice is computationally
318 expensive to evaluate.

319 3.2.1 Markovian Reformulation

320 This section details the formal derivation of the PIROM as a system of ODEs for the thermal
321 dynamics, based on approximations to the memory kernel. Specifically, the kernel $\tilde{\kappa}$ is
322 examined via a leading-order expansion, based on prior work [18]; this can be viewed as an
323 analog of zeroth-order holding in linear system theory with a sufficiently small time step. In
324 this case, the memory kernel is approximated as,

$$\tilde{\kappa}(t, s, \bar{\mathbf{u}}) \approx \mathbf{r}^{(1)}(\bar{\mathbf{u}}, t) \cdot \nabla_{\bar{\mathbf{u}}} \mathbf{r}^{(2)}(\Phi \bar{\mathbf{u}}, t) \quad (27)$$

325 Note that the terms in $\mathbf{r}^{(1)}$ have a common factor $\bar{\mathbf{A}}^{-1}$; this motivates the following heuristic
326 modification of the model form in eq. (26),

$$\dot{\bar{\mathbf{u}}} = \mathbf{r}^{(1)}(\bar{\mathbf{u}}, t) + \bar{\mathbf{A}}^{-1}(\bar{\mathbf{u}}) \int_0^t \kappa(t, s, \bar{\mathbf{u}}) ds \quad (28a)$$

$$\bar{\mathbf{A}}(\bar{\mathbf{u}}) \dot{\bar{\mathbf{u}}} = \bar{\mathbf{B}}(\bar{\mathbf{u}}) \bar{\mathbf{u}} + \bar{\mathbf{f}}(t) + \int_0^t \kappa(t, s, \bar{\mathbf{u}}) ds \quad (28b)$$

327 where the original kernel $\tilde{\kappa}$ is effectively normalized by $\bar{\mathbf{A}}^{-1}$. Intuitively, such choice of kernel
328 reduces its dependency on the averaged material properties, and simplifies the subsequent
329 design of model form.

330 Subsequently, the hidden states are introduced to ‘‘Markovianize’’ the system eq. (26).
331 In this manner, eq. (28b) is converted into a pure state-space model, with the functional
332 form of the LCM retained; since LCM is a physics-based model, then it encodes the phys-
333 ical information and retains explicit parametric dependence of the problem. Consider the
334 representation of the kernel as a finite sum of simpler functions, e.g., exponentials,

$$\kappa(t, s, \bar{\mathbf{u}}) = \sum_{j=1}^m \mathcal{K}_j(t, s, \bar{\mathbf{u}}) [\mathbf{p}_j + \mathbf{d}_j(\bar{\mathbf{u}})] \phi_j(s, \bar{\mathbf{u}}) \quad (29)$$

335 where,

$$\mathcal{K}_j(t, s, \bar{\mathbf{u}}) = e^{-\int_s^t (\lambda_j + e_j(\bar{\mathbf{u}})) d\tau}, \quad \phi_j(s, \bar{\mathbf{u}}) = \mathbf{q}_j^\top \bar{\mathbf{u}}(s) + \mathbf{g}_j(\bar{\mathbf{u}})^\top \bar{\mathbf{u}}(s) + \mathbf{r}_j^\top \bar{\mathbf{f}}(s) \quad (30)$$

³³⁶ with suitable coefficients $\mathbf{p}_j, \mathbf{d}_j, \mathbf{q}_j, \mathbf{g}_j, \mathbf{r}_j \in \mathbb{R}^N$ and decay rates $\lambda_j, e_j(\bar{\mathbf{u}}) > 0$, that need to
³³⁷ be identified from data.

³³⁸ Define the hidden states as,

$$\beta_j(t) = \int_0^t \mathcal{K}_j(s, \bar{\mathbf{u}}) \phi_j(s, \bar{\mathbf{u}}) ds \quad (31)$$

³³⁹ and differentiate with respect to time,,

$$\dot{\beta}_j(t) = -[\lambda_j + e_j(\bar{\mathbf{u}})] \beta_j(t) + \mathbf{q}_j^\top \bar{\mathbf{u}}(t) + \mathbf{g}_j(\bar{\mathbf{u}})^\top \bar{\mathbf{u}}(t) + \mathbf{r}_j^\top \bar{\mathbf{f}}(t) \quad (32)$$

³⁴⁰ to obtain the memory,

$$\int_0^t \boldsymbol{\kappa}(t, s, \bar{\mathbf{u}}) ds = \sum_{j=1}^m [\mathbf{p}_j + \mathbf{d}_j(\bar{\mathbf{u}})] \beta_j(t) \quad (33)$$

³⁴¹ Then, eq. (28b) is recast as the extended Markovian system,

$$\bar{\mathbf{A}}(\bar{\mathbf{u}}) \dot{\bar{\mathbf{u}}} = \bar{\mathbf{B}}(\bar{\mathbf{u}}) \bar{\mathbf{u}} + [\mathbf{P} + \mathbf{D}(\bar{\mathbf{u}})] \boldsymbol{\beta} + \bar{\mathbf{f}}(t) \quad (34a)$$

$$\dot{\boldsymbol{\beta}} = [\mathbf{Q} + \mathbf{G}(\bar{\mathbf{u}})] \bar{\mathbf{u}} + [\mathbf{E}(\bar{\mathbf{u}}) - \boldsymbol{\Lambda}] \boldsymbol{\beta} + \mathbf{R} \bar{\mathbf{f}}(t) \quad (34b)$$

³⁴² where the data-driven operators associated to the hidden dynamics are collected as,

$$\boldsymbol{\Lambda} = \text{diag}(\lambda_1, \lambda_2, \dots, \lambda_m) \in \mathbb{R}^{m \times m}, \quad \mathbf{P} = [\mathbf{p}_1, \mathbf{p}_2, \dots, \mathbf{p}_m] \in \mathbb{R}^{N \times m} \quad (35a)$$

$$\mathbf{D}(\bar{\mathbf{u}}) = [\mathbf{d}_1(\bar{\mathbf{u}}), \mathbf{d}_2(\bar{\mathbf{u}}), \dots, \mathbf{d}_m(\bar{\mathbf{u}})] \in \mathbb{R}^{N \times m}, \quad \mathbf{Q} = [\mathbf{q}_1, \mathbf{q}_2, \dots, \mathbf{q}_m] \in \mathbb{R}^{m \times N} \quad (35b)$$

$$\mathbf{G}(\bar{\mathbf{u}}) = [\mathbf{g}_1(\bar{\mathbf{u}}), \mathbf{g}_2(\bar{\mathbf{u}}), \dots, \mathbf{g}_m(\bar{\mathbf{u}})] \in \mathbb{R}^{m \times N}, \quad \mathbf{R} = [\mathbf{r}_1, \mathbf{r}_2, \dots, \mathbf{r}_m] \in \mathbb{R}^{m \times N} \quad (35c)$$

$$\mathbf{E}(\bar{\mathbf{u}}) = \text{diag}(e_1(\bar{\mathbf{u}}), e_2(\bar{\mathbf{u}}), \dots, e_m(\bar{\mathbf{u}})) \in \mathbb{R}^{m \times m} \quad (35d)$$

³⁴³ The form of the temperature-dependent matrices $\mathbf{D}(\bar{\mathbf{u}})$, $\mathbf{G}(\bar{\mathbf{u}})$, and $\mathbf{E}(\bar{\mathbf{u}})$ is specified in the
³⁴⁴ next section. Since the hidden states $\boldsymbol{\beta}$ serve as the memory, their initial conditions are set
³⁴⁵ to zero, i.e., $\boldsymbol{\beta}(t_0) = \mathbf{0}$, no memory at the beginning. The physics-infused model in eq. (34)
³⁴⁶ retains the structure of the LCM, while the hidden states account for missing physics through
³⁴⁷ corrections to the stiffness and advection matrices, as well as the forcing term.

³⁴⁸ 3.2.2 Coupled Physics-Infused Model

³⁴⁹ The next step involves coupling the physics-infused model in eq. (34) with the SRM in
³⁵⁰ eq. (13) to define the PIROM for ablating TPS. To this end, define the observables as the
³⁵¹ surface temperature $\mathbf{z}_u \in \mathbb{R}^{\tilde{N}}$ and displacements $\mathbf{z}_w \in \mathbb{R}^{\tilde{N}}$ for $\tilde{N} \leq N$ ablating components
³⁵² to define the observable vector as $\mathbf{z} = [\mathbf{z}_u, \mathbf{z}_w]^\top \in \mathbb{R}^{n_z}$ with $n_z = 2\tilde{N}$ as the total number of
³⁵³ observables.

³⁵⁴ Collect the RPM and hidden states into a single state vector $\mathbf{y} = [\bar{\mathbf{u}}, \mathbf{w}, \boldsymbol{\beta}]^\top \in \mathbb{R}^{n_y}$, where
³⁵⁵ $n_y = N + \tilde{N} + m$, and define a data-driven operator $\mathbf{M} \in \mathbb{R}^{n_z \times n_y}$ to define the PIROM's
³⁵⁶ observable as,

$$\mathbf{z} = \mathbf{M} \mathbf{y} \quad (36)$$

³⁵⁷ where,

$$\mathbf{M} = \begin{bmatrix} \mathbf{M}_{\bar{u}} & \mathbf{0} & \mathbf{M}_{\beta} \\ \mathbf{0} & \mathbf{I} & \mathbf{0} \end{bmatrix} \quad (37)$$

³⁵⁸ includes the matrices $\mathbf{M}_{\bar{u}} \in \mathbb{R}^{\tilde{N} \times N}$ and $\mathbf{M}_{\beta} \in \mathbb{R}^{\tilde{N} \times m}$, which computes the surface tempera-
³⁵⁹ ture observable from the RPM states and hidden states, respectively. The PIROM is coupled
³⁶⁰ to the SRM in eq. (13) by leveraging eq. (36) to compute the surface recession velocity. Thus,
³⁶¹ the PIROM is formally stated as,

$$\mathcal{A}\dot{\mathbf{y}} = [\mathcal{B} + \mathcal{C}] \mathbf{y} + \mathcal{F}(t) \quad (38a)$$

$$\mathbf{z} = \mathbf{M}\mathbf{y} \quad (38b)$$

³⁶² where,

$$\mathcal{A} = \begin{bmatrix} \bar{\mathbf{A}} & \mathbf{O} & \mathbf{O} \\ \mathbf{O} & \mathbf{I} & \mathbf{O} \\ \mathbf{O} & \mathbf{O} & \mathbf{I} \end{bmatrix} \in \mathbb{R}^{n_y \times n_y}, \quad \mathcal{B} = \begin{bmatrix} \bar{\mathbf{B}} & \mathbf{O} & \mathbf{P} \\ \Xi\mathbf{M}_u & \mathbf{O} & \Xi\mathbf{M}_{\beta} \\ \mathbf{Q} & \mathbf{O} & -\Lambda \end{bmatrix} \in \mathbb{R}^{n_y \times n_y}, \quad (39a)$$

$$\mathcal{C} = \begin{bmatrix} \mathbf{O} & \mathbf{O} & \mathbf{D}(\bar{\mathbf{u}}) \\ \mathbf{O} & \mathbf{O} & \mathbf{O} \\ \mathbf{G}(\bar{\mathbf{u}}) & \mathbf{O} & \mathbf{E}(\bar{\mathbf{u}}) \end{bmatrix} \in \mathbb{R}^{n_y \times n_y}, \quad \mathcal{F} = \begin{bmatrix} \bar{\mathbf{f}}(t) \\ -\tilde{\mathbf{f}} \\ \mathbf{R}\bar{\mathbf{f}}(t) \end{bmatrix} \in \mathbb{R}^{n_y} \quad (39b)$$

³⁶³ The learnable parameters in the PIROM are collected as,

$$\Theta = \{\mathbf{P}, \mathbf{Q}, \mathbf{R}, \mathbf{D}(\bar{\mathbf{u}}), \mathbf{G}(\bar{\mathbf{u}}), \mathbf{E}(\bar{\mathbf{u}}), \mathbf{M}_u, \mathbf{M}_{\beta}\}, \in \mathbb{R}^{n_{\theta}} \quad (40)$$

³⁶⁴ Particularly, the matrices $\mathbf{P}, \Lambda, \mathbf{Q}, \mathbf{R}$ are constants that need to be identified from data, and
³⁶⁵ account for the effects of coarse-graining on the stiffness and forcing matrices. The matrices
³⁶⁶ $\mathbf{D}(\bar{\mathbf{u}}), \mathbf{E}(\bar{\mathbf{u}}), \mathbf{G}(\bar{\mathbf{u}})$ are state-dependent matrices, and account for the effects of coarse-graining
³⁶⁷ on the advection matrix due to mesh motion. Leveraging the DG-FEM formula for the
³⁶⁸ advection matrix in eq. (55c) in the Appendix, and noting that the ablating velocity in
³⁶⁹ eq. (4) imposes the boundary condition for the mesh motion, the state-dependent matrices
³⁷⁰ for the i -th component are written as,

$$\mathbf{D}(\bar{\mathbf{u}}) \approx \dot{\mathbf{w}}(\bar{\mathbf{u}}) \odot_r \mathbf{D}, \quad \mathbf{G}(\bar{\mathbf{u}}) \approx \mathbf{G} \odot_r \dot{\mathbf{w}}(\bar{\mathbf{u}}), \quad \mathbf{E}(\bar{\mathbf{u}}) \approx \dot{\mathbf{W}}(\bar{\mathbf{u}}) \odot \mathbf{E} \quad (41)$$

³⁷¹ where $\dot{\mathbf{w}}(\bar{\mathbf{u}})$ is the SRM based on the observable temperature $\bar{\mathbf{u}}$, \odot_r is the row-wise multipli-
³⁷² cation, and $\dot{\mathbf{W}}$ is the concatenation of $\dot{\mathbf{w}}$ for \tilde{m} times, where \tilde{m} corresponds to the number
³⁷³ of hidden states per component, i.e., $m = N\tilde{m}$.

³⁷⁴ The PIROM in eq. (38) incorporates explicit information on the material properties,
³⁷⁵ boundary conditions, and surface recession, and is designed to generalize across parametric
³⁷⁶ variations in these inputs. Moreover, the hidden dynamics in eq. (34) are interpretable, as
³⁷⁷ these retain the functional form of the DG-FEM in eq. (8). The next step is focused on
³⁷⁸ identifying the unknown data-driven parameters Θ characterizing the hidden dynamics.

379 3.3 Learning the Hidden Dynamics

- 380 Learning of the PIROM is achieved through a gradient-based neural-ODE-like approach [3].
 381 For ease of presentation, consider the compact form of the PIROM in eq. (38),

$$\mathcal{D}(\dot{\mathbf{y}}, \mathbf{y}, \boldsymbol{\xi}, \mathcal{F}; \Theta) = \mathbf{0} \quad (42)$$

382 where $\boldsymbol{\xi}$ defines the model parameters, i.e., material properties and B' tables, while \mathcal{F}
 383 represents the forcing terms, i.e., the boundary conditions.

384 Consider a dataset of N_s high-fidelity *surface temperature* observable trajectories \mathbf{z}_{HF} ,
 385 sampled at p time instances $\{t_k\}_{k=0}^{p-1}$, for different parameter settings $\{\boldsymbol{\xi}^{(l)}\}_{l=1}^{N_s}$ and forcing
 386 functions $\{\mathcal{F}^{(l)}(t)\}_{l=1}^{N_s}$. The dataset is expressed as,

$$\mathcal{D} = \left\{ \left(t_k, \mathbf{z}_{\text{HF}}^{(l)}(t_k), \boldsymbol{\xi}^{(l)}, \mathcal{F}^{(l)}(t_k) \right) \right\}_{l=1}^{N_s}, \quad k = 0, 1, \dots, p-1 \quad (43)$$

387 In this work, the dataset contains only surface temperature observables – all high-fidelity
 388 information regarding the surface displacements *are assumed to be unavailable during learning*.

389 The learning problem is formulated as the following differentially-constrained problem,

$$\min_{\Theta} \quad \mathcal{J}(\Theta; \mathcal{D}) = \sum_{l=1}^{N_s} \int_{t_0}^{t_f} \ell \left(\mathbf{z}_u^{(l)}, \mathbf{z}_{\text{HF}}^{(l)} \right) dt \quad (44a)$$

$$\text{s.t.} \quad \mathbf{0} = \mathcal{D} \left(\dot{\mathbf{y}}^{(l)}, \mathbf{y}^{(l)}, \boldsymbol{\xi}^{(l)}, \mathcal{F}^{(l)}; \Theta \right) \quad (44b)$$

391 for $l = 1, 2, \dots, N_s$, the objective is to minimize the discrepancy between the high-fidelity
 392 and PIROM predictions for the l -th trajectory with $\ell \left(\mathbf{z}_u^{(l)}, \mathbf{z}_{\text{HF}}^{(l)} \right) = \left\| \mathbf{z}_u^{(l)} - \mathbf{z}_{\text{HF}}^{(l)} \right\|_2^2$.

393 The gradient-based optimization loop is based on the adjoint variable $\boldsymbol{\lambda}$, governed by the
 394 adjoint differential equation,

$$\frac{\partial \ell}{\partial \mathbf{y}} + \boldsymbol{\lambda}^\top \frac{\partial \mathcal{D}}{\partial \mathbf{y}} - \frac{d}{dt} \left(\boldsymbol{\lambda}^\top \frac{\partial \mathcal{D}}{\partial \dot{\mathbf{y}}} \right) = \mathbf{0} \quad (45a)$$

$$\boldsymbol{\lambda}(t_f)^\top \frac{\partial \mathcal{D}}{\partial \dot{\mathbf{y}}(t_f)} = \mathbf{0} \quad (45b)$$

395 Once $\boldsymbol{\lambda}$ is solved, the gradient is computed as,

$$\nabla_{\Theta} \mathcal{J} = \frac{1}{N_s} \sum_{l=1}^{N_s} \int_{t_0}^{t_f} \left(\frac{\partial \ell}{\partial \Theta} + (\boldsymbol{\lambda}^{(l)})^\top \frac{\partial \mathcal{D}}{\partial \Theta} \right) dt \quad (46)$$

396 4 Application to Thermal Protection Systems

397 In this section, the proposed PIROM approach is applied to the analysis of thermo-ablative
 398 multi-layered hypersonic TPS. The performance of the PIROM is evaluated in terms of the

Component	w (cm)	h (cm)	ρ (kg/m ³)	c_p (J/kg·K)	k (W/m·K)	$\alpha \times 10^{-6}$ (m/s·K)
#1	0.3	0.03	160	1200	0.2	1
#2	0.3	0.03	1800	900	5	1
#3	0.3	0.03	300	1500	0.15	1
#4	0.9	0.03	1600	800	10	0

Table 1: Description of TPS components, including thickness h , density ρ , specific heat capacity c_p , thermal conductivity k , and SRM parameter α .

399 three corners of the ITM in Fig. across a wide range of boundary condition and SRM
400 model parametrizations. The results show PIROM to be a promising candidate for the
401 solution of the impossible trinity of modeling.

402 4.1 Problem Definition

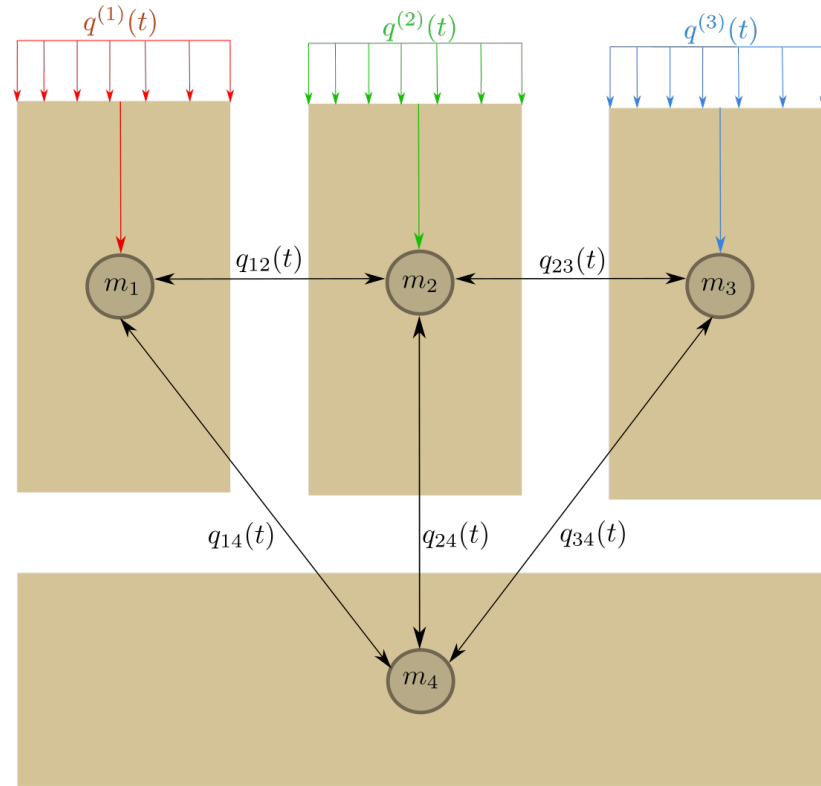
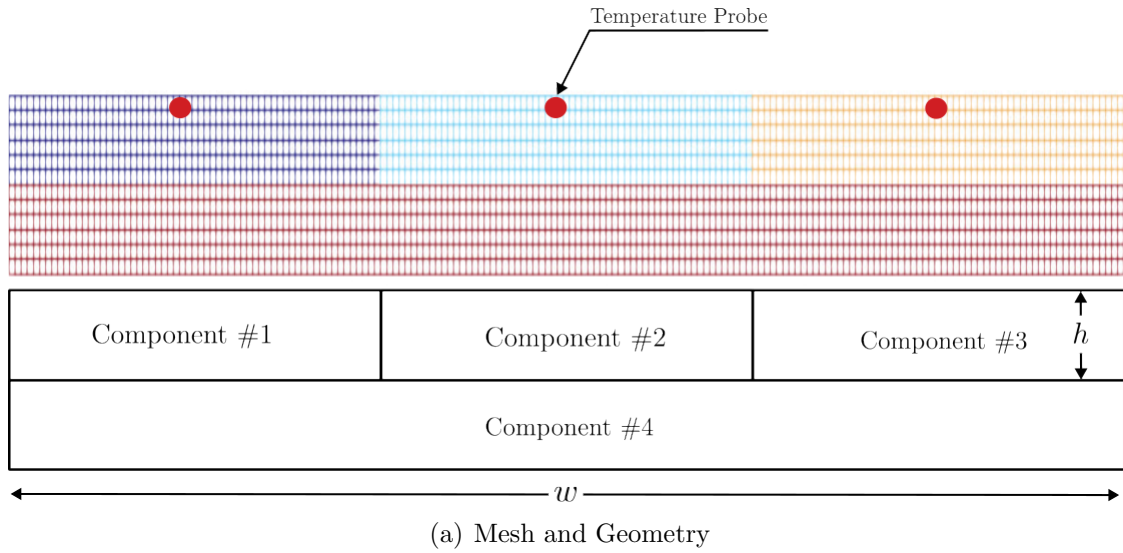
403 Consider the two-dimensional TPS configuration shown in Fig. 3 with constant material
404 properties within each layer, dimensions, and BCs listed in Table 1. Such configuration is
405 representative of the TPS used for the initial concept 3.X vehicle in past studies [10], and in-
406 volves two main layers: an outer ablative layer, and an inner substrate layer. The top ablative
407 layer may be composed of different materials, such as PICA or Avcoat, while the substrate
408 layer is typically made of a high-temperature resistant material, such as carbon-carbon com-
409 posite [7]. The ablative layer, composed of $\tilde{N} = 3$ ablative components, is subjected to
410 strong time-varying and non-uniform heating, while the substrate layer, composed of one
411 non-ablative component, is insulated adiabatically at the outer surface; the total number of
412 components is thus $N = 4$.

413 The lumped-mass representation of the TPS configuration is shown in Fig. 3(b), where
414 each component Ω_i is represented by a lumped mass with uniform temperature $u_i(t)$. Details
415 regarding the derivation of the LCM for this configuration are provided in Appendix A.
416 The sources of non-linearities studied in this problem originate from the coupling between
417 the thermodynamics and temperature-dependent mesh motion, i.e., geometry-dependent
418 matrices, as well as the heterogeneities across material layers. As shown in Fig. 3, perfect
419 thermocouple devices are placed at the surfaces of the ablative layers for the collection of
420 the high-fidelity temperature signals that are used in the following sections for training and
421 testing the PIROM.

422 4.2 Problem Parametrization

423 The operating conditions of the TPS are specified by the boundary conditions, i.e., the heat
424 flux, and the surface recession model (SRM). Specifically, the heat flux on the Neumann
425 BC is parametrized using $\boldsymbol{\xi}_{\text{BC}} = \{\xi_0, \xi_1, \xi_2\}$, while the SRM is parametrized using $\boldsymbol{\xi}_{\text{SRM}} =$
426 $\{\alpha_1, \alpha_2, \alpha_3\}$. Thus, the heat flux and SRM over the i -th ablative component are expressed
427 as,

$$q(x, t; \boldsymbol{\xi}_{\text{BC}}) = \xi_0 e^{\xi_1 x} e^{\xi_2 t}, \forall x \in \Gamma_{i,q}, \quad \dot{w}_i(z_{u,i}; \boldsymbol{\xi}_{\text{SRM}}) = \alpha_i (z_{u,i} - u_{0,i}) \quad (47)$$



(b) Lumped Mass Representation

Figure 3: Four-component TPS geometry and lumped-mass representation for the TPS.

428 where $\Gamma_{i,q}$, $z_{u,i}$, and $u_{0,i}$ correspond to the Neumann BC surface, the PIROM's surface tem-
 429 perature prediction, and the initial temperature of the i -th ablative component, respectively.
 430 The parameters ξ_0 , ξ_1 , and ξ_2 control the heat flux magnitude, spatial variation, and temporal
 431 variation, respectively. The constant α_i is a small material-dependent constant determined
 432 from the B' table [12], specifying the surface recession velocity for a given change in surface
 433 temperature.

434 4.3 Data Generation

435 Full-order solutions of the TPS are computed using the FEM multi-mechanics module of
 436 the **Aria** package [4], where the mesh is shown in Fig. 3. The mesh consists of 2196 to-
 437 tal elements, with 366 elements for each ablative component and 1098 elements for the
 438 substrate component. All solutions are computed for one minute from an uniform ini-
 439 tial temperature of $T(x, t_0) = 300$ K. Given an operating condition $\boldsymbol{\xi} = [\boldsymbol{\xi}_{\text{BC}}, \boldsymbol{\xi}_{\text{SRM}}]^\top$, a
 440 full-order solution consists of then collection of time-varying temperature and displacement
 441 fields $\left\{ \left(t_k, \mathbf{u}_{\text{HF}}^{(l)}(t_k), \mathbf{w}_{\text{HF}}^{(l)}(t_k), \boldsymbol{\xi}^{(l)} \right) \right\}_{k=0}^{p-1}$, where p is the number of time steps with a step size
 442 of $\Delta t \approx 10^{-3}$. The observable trajectories are representative of near-wall thermocouple
 443 sensing of hypersonic flows involving heat transfer. At each time instance t_k , a tempera-
 444 ture reading is recorded from each ablative component using the thermocouples shown in
 445 Fig. 3, resulting in three temperature signals, i.e., the observables $\mathbf{z}_{textHF} \in \mathbb{R}^3$. Therefore,
 446 each full-order solution produces one trajectory of observables $\left\{ \left(t_k, \mathbf{z}_{\text{HF}}^{(l)}(t_k), \boldsymbol{\xi}^{(l)} \right) \right\}_{k=0}^{p-1}$. The
 447 goal of the PIROM is to predict the surface temperature and displacement as accurately as
 448 possible.

449 4.3.1 Definition of Training and Testing Datasets

450 The range of parameters used to generate the training \mathcal{D}_1 and testing $\{\mathcal{D}_2, \mathcal{D}_3\}$ datasets
 451 are listed in Table 1. The training and testing datasets are designed, respectively, to: (1)
 452 minimize the information that the PIROM can “see”, and (2) to maximize the variabil-
 453 ity of test operating conditions to examine the PIROM’s generalization performance. A
 454 total of 110 normally-distributed data points for the BC parametrization are visualized in
 455 Fig. 4(a), and the corresponding observable trajectories are shown in Figs. 4(b) and 4(c).
 456 The training dataset \mathcal{D}_1 includes 10 trajectories with randomly selected BC parameters from
 457 the 110 points, with nominal SRM parameters $\boldsymbol{\xi}_{\text{SRM}} = \{1, 1, 1\} \times 10^{-6}$. Note that although
 458 Fig. 4(c) shows the surface displacements for all ablative components in \mathcal{D}_1 , only the *surface*
 459 *temperature is used for training the PIROM.*

460 Two additional datasets are generated for testing. The dataset \mathcal{D}_2 includes the remaining
 461 100 BC parameter values not considered in \mathcal{D}_1 , and the high-fidelity simulation are generated
 462 with the same nominal SRM parameters. The cases in the \mathcal{D}_3 fixes the boundary condition
 463 as shown in Fig. 4(a) and varies the SRM parameters as shown in Table. 1. The testing
 464 datasets \mathcal{D}_2 and \mathcal{D}_3 are *out-of-distribution* (OOD) datasets, and are meant for testing the
 465 generalizability of the ROMs to unseen BCs and SRMs, respectively.

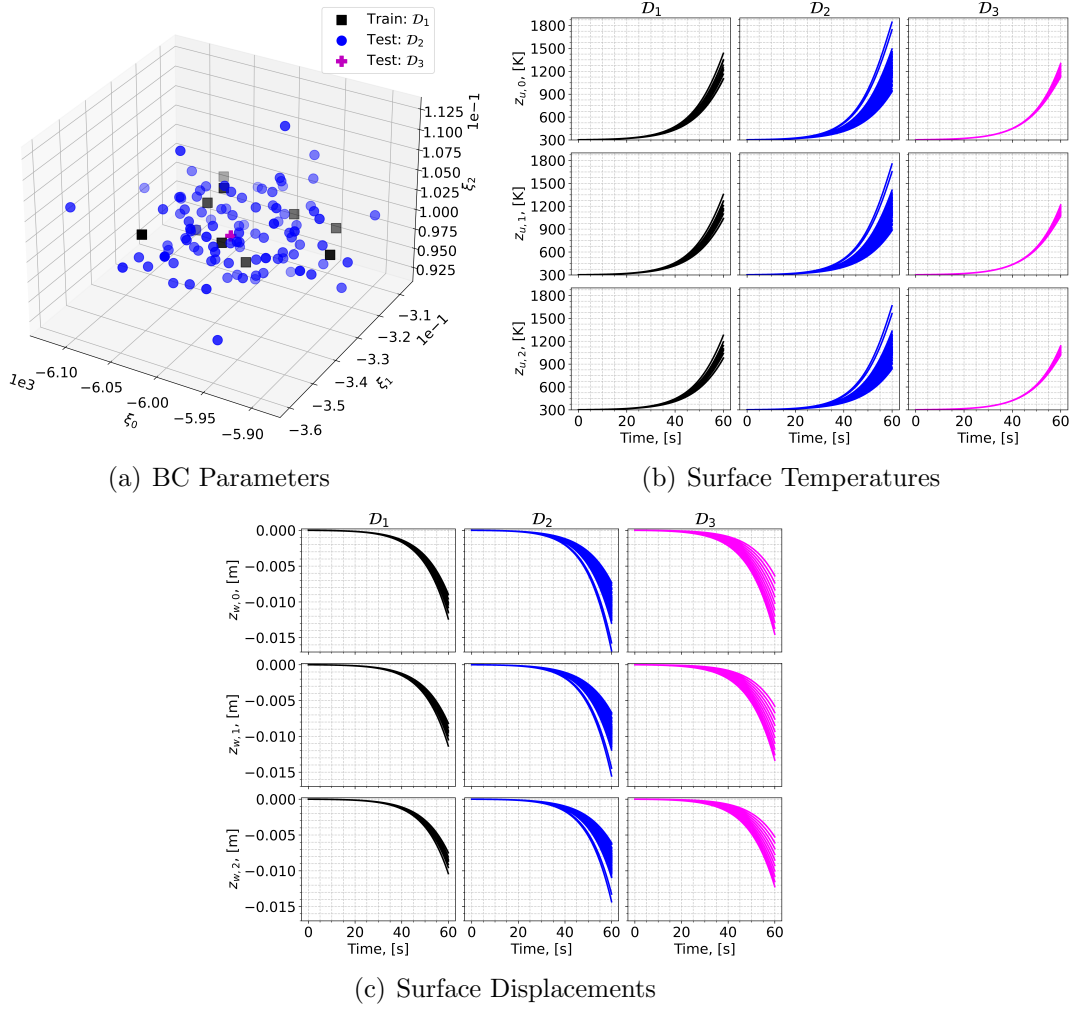


Figure 4: Boundary condition parameters, temperature observables, and displacement observables for the training and testing datasets. The variables $z_{u,i}$ and $z_{w,i}$ correspond to the surface temperature and displacement of the i -th ablative component, respectively.

466 4.4 Performance Metrics

467 The performance of the PIROM is evaluated by the metrics of prediction error and compu-
 468 tational cost.

469 **Prediction Error** Consider one trajectory of high-fidelity surface temperature and dis-
 470 placement data $\left\{ \left(t_k, \mathbf{z}_{u,\text{HF}}^{(l)}(t_k), \mathbf{z}_{w,\text{HF}}^{(l)}(t_k) \right) \right\}_{k=0}^{p-1}$ for the l -th operating condition in the testing
 471 datasets \mathcal{D}_2 or \mathcal{D}_3 . The difference $e_i^{(l)}$ for the i -th predicted observable, denoted as $z_i^{(l)}$, is
 472 computed as,

$$e_i^{(l)} = \frac{1}{\Delta z_i^{(l)}} \sqrt{\frac{1}{p} \sum_{k=0}^{p-1} \left(z_{i,\text{HF}}^{(l)}(t_k) - z_i^{(l)}(t_k) \right)^2} \quad (48)$$

473 for $i = 1, 2, 3$ and $z_i^{(l)} \in \left\{ z_{i,u}^{(l)}, z_{i,w}^{(l)} \right\}$, and where,

$$\Delta z_i^{(l)} = \max_{0 \leq k \leq p-1} z_{i,\text{HF}}^{(l)}(t_k) - \min_{0 \leq k \leq p-1} z_{i,\text{HF}}^{(l)}(t_k) \quad (49)$$

474 Subsequently, the prediction error of one trajectory is computed by a weighted sum based
 475 on the area of each *ablative component*, resulting in the normalized root mean square error
 476 (NRMSE) metric for one trajectory,

$$\text{NRMSE} = \frac{\sum_{i=1}^{\tilde{N}} |\Omega_i| e_i^{(l)}}{\sum_{i=1}^{\tilde{N}} |\Omega_i|} \times 100\% \quad (50)$$

477 For one dataset, the NRMSE is defined to be the average of the NRMSEs of all trajectories
 478 in the dataset.

479 **Computational Acceleration** The *computational acceleration* metric focuses on the quan-
 480 tification of the speedup factor $\frac{\mathcal{T}_{\text{HF}}(\mathcal{D})}{\mathcal{T}_{\mathcal{M}}(\mathcal{D})}$, where $\mathcal{T}_{\text{HF}}(\mathcal{D})$ and $\mathcal{T}_{\mathcal{M}}(\mathcal{D})$ correspond to the wall-clock
 481 time required by the high-fidelity model and the reduced-order model \mathcal{M} (i.e., PIROM or
 482 RPM) to evaluate all trajectories in the dataset \mathcal{D} , respectively. For a benchmark analysis
 483 of the computational costs during the training phase, please refer to Ref. [16].

484 4.5 Generalization to Boundary Conditions

485 To assess generalization to BC, the PIROM and RPM are evaluated on the \mathcal{D}_2 dataset. Tem-
 486 perature trajectory predictions for a representative test case are shown in Figs. 5(a) and 5(b),
 487 where the PIROM accurately captures the surface temperature and displacement dynamics,
 488 while the RPM exhibits larger deviations and under-predicts surface displacements due to
 489 the averaging effects of the LCM. The mean NRMSE across all test cases in \mathcal{D}_2 is shown
 490 in Figs. 5(e) and 5(f), where the PIROM consistently achieves errors of $\approx 0.5\%$ for both
 491 temperature and displacement predictions, improving the RPM's accuracy by an order of
 492 magnitude. Figure 5 reports the average substrate temperature, where the LCM remains
 493 highly accurate due to the symmetric TPS geometry, adiabatic BCs, and negligible thermal

494 gradients within the substrate. Although the PIROM is trained only on the surface tem-
495 peratures of the three ablative components, its hidden dynamics retain the LCM’s accuracy
496 for this untrained observable, demonstrating the PIROM’s ability to generalize and preserve
497 the underlying physics of the reduced-physics backbone.

498 4.6 Generalization to Surface Recession Models

499 The generalization performance of the PIROM and RPM is also evaluated on surface reces-
500 sion models using the \mathcal{D}_3 dataset. As detailed in Table 1, the SRM parameter α in \mathcal{D}_3 is
501 perturbed 10 times by up to $\pm 50\%$ from their nominal values. The SRM model perturbation
502 introduces significant changes to the ablative layer dynamics, potentially increasing the rate
503 of ablation at lower temperatures, as shown in Figs. 5(c) and 5(d). The PIROM, without
504 considering any SRM variations during training, is able to accurately predict the surface tem-
505 perature and displacement dynamics for the perturbed SRMs. Figures 5(e) and 5(f) show
506 the mean NRMSE across all test cases in \mathcal{D}_3 , where the PIROM consistently achieves errors
507 below 1.5% for both temperature and displacement predictions, and consistently improves
508 the RPM’s accuracy by approximately an order of magnitude.

509 4.7 Computational Cost

510 All computations are performed in serial for fairness on an Intel Xeon (R) Gold 6258R
511 CPU 2.70GHz computer with 62 GB of RAM. The numerical integration for the RPM
512 and PIROM models are performed using SciPy’s `solve_ivp` function with default settings.
513 Provided a parametrization for the BC and SRM, the high-fidelity FEM simulation takes
514 about ≈ 60 seconds, the RPM takes about ≈ 0.137 seconds, and the PIROM takes about
515 ≈ 0.280 seconds. Therefore, during evaluation both the RPM and PIROM achieve speedup
516 factors of approximately 438 and 214, respectively, over the high-fidelity model. As a result,
517 the PIROM and RPM are *two-orders-of-magnitude faster* than the high-fidelity model. The
518 PIROM nearly preserves the computational efficiency of the RPM (about twice as expensive
519 as the RPM), while achieving significantly higher accuracy and generalization capabilities.
520 The results demonstrate the benefits of physics-infused modeling for the development of
521 efficient and generalizable ROMs for complex multi-physics systems.

522 4.8 Summary of Results

523 The results presented in this section demonstrate the accuracy, generalizability, and com-
524 putational efficiency of the proposed PIROM approach for the analysis of thermo-ablative
525 multi-layered hypersonic TPS. The PIROM consistently achieves low prediction errors below
526 1% for both surface temperature and displacement across a range of unseen boundary con-
527 ditions and surface recession models. Furthermore, the PIROM retains the computational
528 efficiency of traditional RPMs, achieving speedup factors of over 200 times compared to high-
529 fidelity FEM simulations. The generalization capabilities of the PIROM are attributed to its
530 hybrid structure: a physics-based LCM backbone that ensures consistency with the under-
531 lying thermodynamics, while a data-driven correction mechanism captures the un-resolved
532 dynamics.

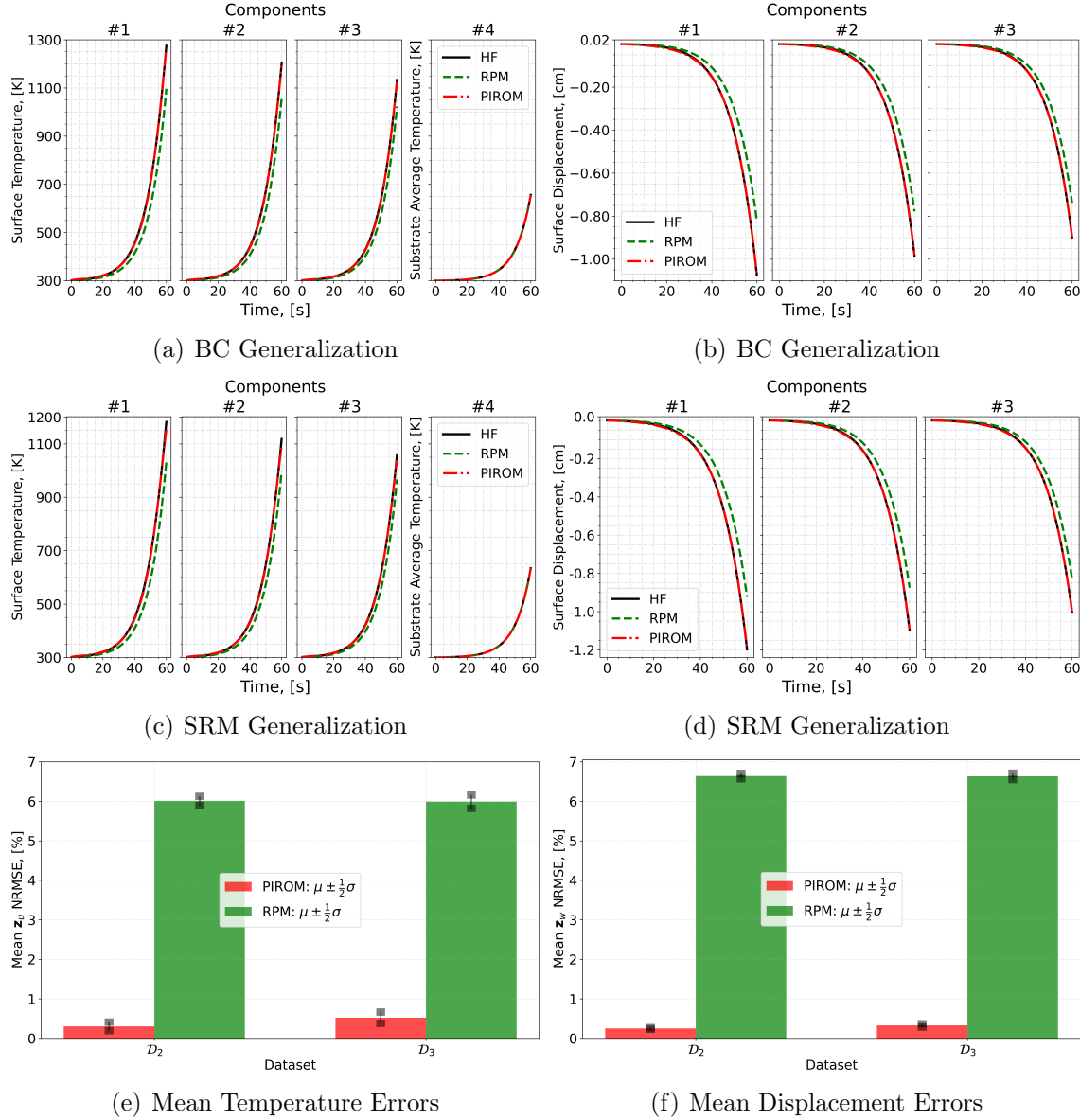


Figure 5: PIROM predictions against high-fidelity solutions for (a)-(b) BC generalization, (c)-(d) SRM generalization, and (e)-(f) mean errors across testing datasets.

533 5 Conclusions

534 This work presents the development and validation of the *scientific machine learning* frame-
535 work termed *Physics-Informed Reduced Order Model* (PIROM) for simulating the transient
536 thermo-ablative response of hypersonic thermal protection systems (TPS) subjected to hy-
537 personic aerodynamic heating. Using coarse-graining on a DG-FEM model and the Mori-
538 Zwanzig formalism, the PIROM formulation in Ref. [16] is extended to account for non-
539 decomposing ablative material response. The PIROM builds upon the following two key
540 components: (1) a first-order physics-based model, i.e., the LCM and SRM, for low-fidelity
541 predictions of the transient thermo-ablative TPS response; and (2) a data-driven closure to
542 the non-Markovian term in the generalized Langevin equation (GLE). The non-Markovian
543 closure is recast as a set of hidden states that evolve according to a data-driven dynamical
544 system that is learned from a sparse collection of high-fidelity temperature signals.

545 The results demonstrate that the PIROM framework effectively reconciles the trade-
546 offs between accuracy, generalizability, and efficiency of the ITM for simulating ablating
547 hypersonic TPS. The PIROM consistently achieves mean observable prediction errors of
548 $\approx 0.5\%$ for a wide range of extrapolative settings of model parameters, involving time-and-
549 space varying boundary conditions and SRM models. Notably, the PIROM improves the
550 RPM's accuracy by an order of magnitude while preserving its computational efficiency,
551 physical interpretability, and parametric generalizability. Moreover, the PIROM delivers
552 online evaluations that are two orders of magnitude faster than the FOM. These results
553 highlight the PIROM's potential as a promising framework for optimizing multi-physical
554 dynamical systems, such as TPS under diverse operating conditions.

555 **A Technical Details**

556 This appendix presents the technical details of the PIROM framework applied to the TPS
 557 ablation problem. The first section provides the mathematical details for the definition of
 558 the DG-FEM. The second section follows the projection procedures from Ref. [x](#), and demon-
 559 strates the effects of coarse-graining on the advection matrix. The third section presents the
 560 derivation of the LCM model from an energy-conservation perspective.

561 **A.1 Full-Order Model**

562 To obtain the full-order numerical solution, the governing equation is spatially discretized
 563 using variational principles of Discontinuous Galerkin (DG) to result in a high-dimensional
 564 system of ordinary differential equations (ODEs). The DG-FEM model is written in an
 565 element-wise form, which is beneficial for subsequent derivations of the lower-order models.
 566 Note that the choice of DG approach here is mainly for theoretical convenience in the sub-
 567 sequent coarse-graining formulation. In the numerical results, the full-order TPS ablation
 568 simulations is computed using standard FEM instead, and the equivalence between DG and
 569 standard FEM is noted upon their convergence.

570 **A.1.1 Domain Discretization**

571 Consider a conforming mesh partition of the domain, as shown in Fig. [DOMAIN](#), where each
 572 element belongs to one and only one component. Denote the collection of all M elements
 573 as $\{E_i\}_{i=1}^M$. To ease the description of the DG model, a graph structure is employed. The
 574 elements are treated as vertices, the set of which is denoted $\mathcal{V} = \{m\}_{m=1}^M$. Two neighboring
 575 elements, E_i and E_j , are connected by an edge (i, j) , and the shared boundary between them
 576 is denoted e_{ij} . The collection of all edges are denoted \mathcal{E} , and \mathcal{G} is referred to as a graph.
 577 In the graph, the edges are unidirected, meaning if $(i, j) \in \mathcal{E}$ then $(j, i) \in \mathcal{E}$. Furthermore,
 578 denote the neighbors of the i -th element as $\mathcal{N}_i = \{j | (i, j) \in \mathcal{E}\}$. Lastly, for the ease of
 579 notation, introduce two special indices: T for the boundary of an element that overlaps with
 580 the Dirichlet boundary condition, and similarly q for the Neumann boundary condition.

581 **A.1.2 Weak Form of Discontinuous Galerkin Method**

582 Choosing appropriate basis functions ϕ_k and ϕ_l and using the Interior Penalty Galerkin
 583 (IPG) scheme [5], the variational bilinear form for eq. (1a) is,

$$\sum_{i=1}^M a_{\epsilon,i}(\phi_k, \phi_l) = \sum_{i=1}^M L_i(\phi_k) \quad (51)$$

584 where ϵ is an user-specified parameter and,

$$a_{\epsilon,i}(\phi_k, \phi_l) = \int_{E^{(i)}} \left(\rho c_p \phi_k \frac{\partial \phi_l}{\partial t} + \nabla \phi_k \cdot (\mathbf{k} \nabla \phi_l) - \rho c_p \phi_k \mathbf{v} \cdot \nabla \phi_l \right) dE^{(i)} \quad (52a)$$

$$\begin{aligned} &= - \sum_{j \in \mathcal{N}_i \cup \{T_b\}} \int_{e_{ij}} \{ \mathbf{k} \nabla \phi_k \cdot n \} [\phi_l] de_{ij} + \epsilon \sum_{j \in \mathcal{N}_i \cup \{T_b\}} \int_{e_{ij}} \{ \mathbf{k} \nabla \phi_l \cdot n \} [\phi_k] de_{ij} \\ &\quad + \sigma \sum_{j \in \mathcal{N}_i \cup \{T_b\}} \int_{e_{ij}} [\phi_k] [\phi_l] de_{ij} \end{aligned} \quad (52b)$$

$$L_i(v) = \epsilon \sum_{j \in \mathcal{N}_i \cup \{T_b\}} \int_{e_{ij}} (\mathbf{k} \nabla \phi_l \cdot n) T_b de_{ij} + \int_{e_{iq}} \phi_k q_b de_{iq} + \sigma \int_{e_{iT}} \phi_k T_b de_{iT} \quad (52c)$$

585 In the bi-linear form above, the notations $[]$ and $\{ \}$ are respectively the jumps and averages
586 at the boundary e_{ij} share by two elements E_i and E_j ,

$$[u] = u|_{E_i} - u|_{E_j}, \quad \{u\} = \frac{1}{2} \left(u|_{E_i} + u|_{E_j} \right), \quad \text{for } x \in e_{ij} = E_i \cap E_j$$

587 Furthermore, in the bi-linear form, the terms associated with σ are introduced to enforce
588 the Dirichlet boundary conditions; σ is a penalty factor whose value can depend on the size
589 of an element. Depending on the choice of ϵ , the bi-linear form corresponds to symmetric
590 IPG ($\epsilon = -1$), non-symmetric IPG ($\epsilon = 1$), and incomplete IPG ($\epsilon = 0$). All these schemes
591 are consistent with the original PDE and have similar convergence rate with respect to mesh
592 size. In the following derivations, the case $\epsilon = 0$ is chosen for the sake of simplicity.

593 A.1.3 Discontinuous Galerkin Model

594 Next, the DG-based model is written in an element-wise form. For the i -th element, use a
595 set of P trial functions to represent the temperature as in eq. (6). Without loss of generality,
596 the trial functions are assumed to be orthogonal, so that $\int_{E^{(i)}} \phi_k^{(i)}(x) \phi_l^{(i)}(x) dx = |E^{(i)}| \delta_{kl}$,
597 where $|E^{(i)}|$ is the area ($n_d = 2$) or volume ($n_d = 3$) of the i -th element, and δ_{kl} is the
598 Kronecker delta.

599 Using test functions same as trial functions, the dynamics $\mathbf{u}^{(i)}$ is obtained by evaluating
600 the element-wise bi-linear forms,

$$a_{\epsilon,i}(\phi_k^{(i)}, T^{(i)}) = L_i(\phi_k^{(i)}), \quad k = 1, 2, \dots, P \quad (53)$$

601 The above procedure yields,

$$\mathbf{A}^{(i)} \dot{\mathbf{u}}^{(i)} = (\mathbf{B}^{(i)} + \mathbf{C}^{(i)}(t)) \mathbf{u}^{(i)} + \sum_{j \in \mathcal{N}_i \cup \{T_b\}} \left(\mathbf{B}_{ij}^{(i)} \mathbf{u}^{(i)} + \mathbf{B}_{ij}^{(j)} \mathbf{u}^{(j)} \right) + \mathbf{f}^{(i)}(t) \quad (54)$$

602 where for $k, l = 1, 2, \dots, P$,

$$[\mathbf{A}^{(i)}]_{kl} = \int_{E^{(i)}} \rho c_p \phi_k^{(i)} \phi_l^{(i)} dE^{(i)} \quad (55a)$$

$$[\mathbf{B}^{(i)}]_{kl} = - \int_{E^{(i)}} (\nabla \phi_k^{(i)}) \cdot (\mathbf{k} \nabla \phi_l^{(i)}) dE^{(i)} \quad (55b)$$

$$[\mathbf{C}^{(i)}]_{kl} = \int_{E^{(i)}} \rho c_p \phi_k^{(i)} \mathbf{v}^{(i)} \cdot \nabla \phi_l^{(i)} dE^{(i)} \quad (55c)$$

$$[\mathbf{B}_{ij}^{(i)}] = \int_{e_{ij}} \left\{ \mathbf{k} \nabla \phi_k^{(i)} \cdot \hat{n} \right\} \phi_l^{(i)} - \sigma [\phi_k^{(i)}] \phi_l^{(i)} de_{ij} \quad (55d)$$

$$[\mathbf{B}_{ij}^{(j)}] = \int_{e_{ij}} - \left\{ \mathbf{k} \nabla \phi_k^{(i)} \cdot \hat{n} \right\} \phi_l^{(j)} + \sigma [\phi_k^{(i)}] \phi_l^{(j)} de_{ij} \quad (55e)$$

$$[\mathbf{f}^{(i)}]_k = \int_{e_{iq}} \phi_k^{(i)} q_b de_{iq} + \sigma \int_{e_{iT}} \phi_k^{(i)} de_{iT} \quad (55f)$$

603 The matrices $\mathbf{A}^{(i)} \in \mathbb{R}^{P \times P}$, $\mathbf{B}^{(i)} \in \mathbb{R}^{P \times P}$, and $\mathbf{C}^{(i)} \in \mathbb{R}^{P \times P}$ are respectively the capacitance,
604 conductivity, and advection matrices for element i . These matrices depend on ρ , c_p , \mathbf{k} , and
605 \mathbf{v} , and hence can be non-linear functions of $\mathbf{u}^{(i)}$. Since the trial functions are orthogonal, if
606 ρc_p is constant within an element, $\mathbf{A}^{(i)}$ is diagonal; otherwise, \mathbf{A}_i is symmetric and positive
607 definite as $\rho c_p > 0$.

608 For compactness, the element-wise model in eq. (54) is also written in matrix form,

$$\mathbf{A}(\dot{\mathbf{u}}) = [\mathbf{B}(\mathbf{u}) + \mathbf{C}(\mathbf{u})] \mathbf{u} + \mathbf{f}(t) \quad (56)$$

609 where $\mathbf{u} = [\mathbf{u}^{(1)}, \mathbf{u}^{(2)}, \dots, \mathbf{u}^{(M)}]^T \in \mathbb{R}^{MP}$ includes all DG variables, $\mathbf{f} = [\mathbf{f}^{(1)}, \mathbf{f}^{(2)}, \dots, \mathbf{f}^{(M)}]^T \in$
610 \mathbb{R}^{MP} , \mathbf{A} and \mathbf{C} are matrices of M diagonal blocks whose i -th blocks are $\mathbf{A}^{(i)}$ and $\mathbf{C}^{(i)}$, and
611 \mathbf{B} is a matrix of $M \times M$ blocks whose (i, j) -th block is,

$$\mathbf{B}_{ij} = \begin{cases} \mathbf{B}^{(i)} + \sum_{j \in \mathcal{N}_i \cup \{T_b\}} \mathbf{B}_{ij}^{(i)}, & i = j \\ \mathbf{B}_{ij}^{(j)}, & i \neq j \end{cases} \quad (57)$$

612 The dependency of \mathbf{A} , \mathbf{B} , and \mathbf{C} on \mathbf{u} is explicitly noted in eq. (56), which is the source of
613 non-linearity in the current TPS problem. Moreover, the mesh velocity \mathbf{v} varies with space
614 and time, and thus the advection matrix \mathbf{C} varies with time as a function of q_b .

615 A.2 Coarse-Graining of Dynamics

616 The LCM is obtained by coarse-graining the full-order DG-FEM. This coarse-graining proce-
617 dure produces resolved $\mathbf{r}^{(1)}(\mathbf{u}, t)$ and residual $\mathbf{r}^{(2)}(\mathbf{u}, t)$ dynamics as in eq. (23). This section
618 presents the detail derivations and magnitude analysis for the resolved and residual dynam-
619 ics.

620 **A.2.1 Resolved Dynamics**

621 Using eq. (20), the resolved dynamics is computed as follows,

$$\mathbf{r}^{(1)}(\mathbf{u}, t) = \mathcal{P} [\Phi^+ \mathbf{A}(\mathbf{u})^{-1} (\mathbf{B}(\mathbf{u})\mathbf{u} + \mathbf{C}(\mathbf{u})\mathbf{u} + \mathbf{f}(t))] \quad (58a)$$

$$= \Phi^+ \mathbf{A}(\mathbf{P}\mathbf{u})^{-1} \mathbf{P}\mathbf{B}(\mathbf{P}\mathbf{u}) \mathbf{P}\mathbf{u} + \Phi^+ \mathbf{A}(\mathbf{P}\mathbf{u})^{-1} \mathbf{P}\mathbf{C}(\mathbf{P}\mathbf{u}) \mathbf{P}\mathbf{u} \\ + \Phi^+ \mathbf{A}(\mathbf{P}\mathbf{u})^{-1} \mathbf{P}\mathbf{f}(t, \mathbf{P}\mathbf{u}) \quad (58b)$$

$$= \underbrace{\Phi^+ \mathbf{A}(\Phi\bar{\mathbf{u}})^{-1} \Phi}_{\#1} \underbrace{\Phi^+ \mathbf{B}(\Phi\bar{\mathbf{u}}) \Phi\bar{\mathbf{u}}}_{\#2} + \Phi^+ \mathbf{A}(\Phi\bar{\mathbf{u}})^{-1} \Phi \underbrace{\Phi^+ \mathbf{C}(\Phi\bar{\mathbf{u}}) \Phi\bar{\mathbf{u}}}_{\#3} \\ + \Phi^+ \mathbf{A}(\Phi\bar{\mathbf{u}})^{-1} \Phi \underbrace{\Phi^+ \mathbf{f}(t, \Phi\bar{\mathbf{u}})}_{\#4} \quad (58c)$$

622 Detailed derivations for the #1, #2, and #4 terms can be found in Ref. [x]. The effects of
623 coarse-graining on the advection term #3 are analyzed next.

624 **Term #3** The $\mathbf{C}(\mathbf{u}) \in \mathbb{R}^{MP \times MP}$ matrix contains M diagonal of size $P \times P$, since the
625 basis functions are defined locally on each element. Therefore, $[\mathbf{C}(\mathbf{u})]_{ij} = \mathbf{0}$ for all $i \neq j$ with
626 $i, j = 1, 2, \dots, M$. It follows that for $k, l = 1, 2, \dots, N$,

$$[\Phi^+ \mathbf{C}(t, \Phi\bar{\mathbf{u}}) \Phi]_{kl} = \sum_{i=1}^M \sum_{j=1}^M \boldsymbol{\varphi}_i^{k+} [\mathbf{C}(t, \Phi\bar{\mathbf{u}})]_{ij} \boldsymbol{\varphi}_j^l \quad (59a)$$

$$= \sum_{i=1}^M \boldsymbol{\varphi}_i^{k+} [\mathbf{C}(t, \Phi\bar{\mathbf{u}})]_{ii} \boldsymbol{\varphi}_i^l \quad (59b)$$

$$= \sum_{i \in \mathcal{V}_k} \boldsymbol{\varphi}_i^{k+} [\mathbf{C}(t, \Phi\bar{\mathbf{u}})]_{ii} \boldsymbol{\varphi}_i^l \quad (59c)$$

627 where in the second row, the fact that $[\mathbf{C}(\mathbf{u})]_{ij} = 0$ for all $i \neq j$ is used, and in the last row,
628 the fact that $\boldsymbol{\varphi}_i^{k+} = 0$ for all $i \notin \mathcal{V}_k$ is used. Now, considering that $[\mathbf{C}(\mathbf{u})]_{ii}$ has a (1, 1)-th
629 zero element, i.e., $[\mathbf{C}(t, \Phi\bar{\mathbf{u}})]_{ii} = 0$, and that if $k \neq l$ then $i \notin \mathcal{V}_l$ and thus $\boldsymbol{\varphi}_i^l = \mathbf{0}$, it follows
630 that for some index $i \in \mathcal{V}_k$,

$$\boldsymbol{\varphi}_i^{k+} [\mathbf{C}(t, \Phi\bar{\mathbf{u}})]_{ii} \boldsymbol{\varphi}_i^l = \boldsymbol{\varphi}_i^{k+} [\mathbf{C}(t, \Phi\bar{\mathbf{u}})]_{ii} \boldsymbol{\varphi}_i^k = \frac{|E_i|}{|\Omega_k|} [C_{11}(t, \Phi\bar{\mathbf{u}})]_{ii} = 0 \quad (60)$$

631 The matrix $[\Phi^+ \mathbf{C}(t, \Phi\bar{\mathbf{u}}) \Phi]_{kl} = 0$ for all $k, l = 1, 2, \dots, N$, and thus,

$$\bar{\mathbf{C}}(t, \bar{\mathbf{u}}) = \Phi^+ \mathbf{C}(t, \Phi\bar{\mathbf{u}}) \Phi = \mathbf{0} \quad (61)$$

632 as indicated by the LCM in eq. (9).

633 **A.2.2 Magnitude Analysis for Residual Dynamics**

634 Next, the magnitude of the residual dynamics $\mathbf{r}^{(2)}(\mathbf{u}, t)$ is analyzed to pinpoint the missing
635 physics in the LCM. By definition,

$$\mathbf{r}^{(2)}(\mathbf{u}, t) = \dot{\bar{\mathbf{u}}} - \mathbf{r}^{(1)}(\bar{\mathbf{u}}, t) \quad (62a)$$

$$= \Phi^+ \mathbf{r}(\mathbf{u}, t) - \mathbf{r}^{(1)}(\mathbf{u}, t) \quad (62b)$$

$$\begin{aligned} &= \underbrace{\Phi^+ \mathbf{A}(\mathbf{u})^{-1} \mathbf{B}(\mathbf{u}) \mathbf{u} - \bar{\mathbf{A}}(\bar{\mathbf{u}})^{-1} \bar{\mathbf{B}}(\bar{\mathbf{u}}) \bar{\mathbf{u}}}_{\#1} + \underbrace{\Phi^+ \mathbf{A}(\mathbf{u})^{-1} \mathbf{C}(\mathbf{u}) \mathbf{u} - \bar{\mathbf{A}}(\bar{\mathbf{u}})^{-1} \bar{\mathbf{C}}(t, \bar{\mathbf{u}}) \bar{\mathbf{u}}}_{\#2} \\ &\quad + \underbrace{\Phi^+ \mathbf{A}(\mathbf{u})^{-1} \mathbf{f}(t) - \bar{\mathbf{A}}(\bar{\mathbf{u}})^{-1} \bar{\mathbf{f}}(t)}_{\#3} \end{aligned} \quad (62c)$$

636 The magnitude analysis for terms $\#1$ and $\#3$ can be found in Ref. [x]. The analysis for term
637 $\#2$ is presented next. Let $\mathbf{D}(\bar{\mathbf{u}}) = \mathbf{A}(\Phi \bar{\mathbf{u}})^{-1} \mathbf{P} \mathbf{C}(t, \Phi \bar{\mathbf{u}})$, then,

$$\Phi^+ \mathbf{A}(\mathbf{u})^{-1} \mathbf{C}(\mathbf{u}) \mathbf{u} - \bar{\mathbf{A}}(\bar{\mathbf{u}})^{-1} \bar{\mathbf{C}}(t, \bar{\mathbf{u}}) \bar{\mathbf{u}} \quad (63a)$$

$$= \Phi^+ \mathbf{A}(\mathbf{u})^{-1} \mathbf{C}(\mathbf{u}) \mathbf{u} - \Phi^+ \mathbf{A}(\Phi \bar{\mathbf{u}})^{-1} \mathbf{P} \mathbf{C}(t, \Phi \bar{\mathbf{u}}) \Phi \Phi^+ \mathbf{u} \quad (63b)$$

$$= \Phi^+ \mathbf{A}^{-1}(\mathbf{u}) \mathbf{C}(\mathbf{u}) \mathbf{u} - \Phi^+ \mathbf{D}(\bar{\mathbf{u}}) \Phi \Phi^+ \mathbf{u} \quad (63c)$$

$$(63d)$$

638 where $\mathbf{P} = \Phi \Phi^+$. Thus,

$$\|\Phi^+ \mathbf{A}(\mathbf{u})^{-1} \mathbf{C}(\mathbf{u}) \mathbf{u} - \bar{\mathbf{A}}(\bar{\mathbf{u}})^{-1} \bar{\mathbf{C}}(t, \bar{\mathbf{u}}) \bar{\mathbf{u}}\| \quad (64a)$$

$$\leq \|\Phi^+ \mathbf{A}^{-1}(\mathbf{u}) \mathbf{C}(\mathbf{u}) \mathbf{u} - \Phi^+ \mathbf{D}(\bar{\mathbf{u}}) \mathbf{u}\| + \|\Phi^+ \mathbf{D}(\bar{\mathbf{u}}) \mathbf{u} - \Phi^+ \mathbf{D}(\bar{\mathbf{u}}) \Phi \Phi^+ \mathbf{u}\| \quad (64b)$$

$$\leq \|\Phi^+\| \underbrace{\|\mathbf{A}^{-1}(\mathbf{u}) \mathbf{C}(\mathbf{u}) \mathbf{u} - \mathbf{D}(\bar{\mathbf{u}}) \mathbf{u}\|}_{\#1} + \|\Phi^+ \mathbf{D}(\bar{\mathbf{u}})\| \underbrace{\|\mathbf{u} - \Phi \Phi^+ \mathbf{u}\|}_{\#2} \quad (64c)$$

639 where term $\#2$ is due to the approximation of non-uniform temperature as constants, and
640 term $\#1$ is the error in the advection dynamics due to coarse-graining.

641 **A.3 Lumped Capacitance Model**

642 The following assumptions are employed: (1) the temperature in component (i) is described
643 by a scalar time-varying average temperature $\bar{u}^{(i)}$, (2) between neighboring components (i)
644 and (j) the heat flux is approximated as,

$$q_{ij} = \frac{\bar{u}^{(j)} - \bar{u}^{(i)}}{R_{ij}} \quad (65)$$

645 where R_{ij} is the thermal resistance. Empirically, for a component of isotropic heat conduction
646 conductivity k , length ℓ , and cross-section area A , the thermal resistance is $R = \ell/kA$. Between
647 components i and j , define $R_{ij} = R_i + R_j$. In addition, the heat flux due to Dirichlet
648 boundary condition is computed as $q_{iT} = (T_b - \bar{u}^{(i)})/R_i$.

649 At component i , the dynamics of LCM are given by,

$$\int_{E^{(i)}} \rho c_p \dot{\bar{u}}^{(i)} dE^{(i)} = \left(\sum_{j \in \mathcal{N}_i} \int_{e_{ij}} \frac{\bar{u}^{(j)} - \bar{u}^{(i)}}{R_{ij}} de_{ij} \right) + \int_{e_{iq}} q_b de_{iq} + \int_{e_{iT}} \frac{T_b - \bar{u}^{(i)}}{R_i} de_{iT} \quad (66a)$$

$$\bar{A}^{(i)} \dot{\bar{u}}^{(i)} = \left(\sum_{j \in \mathcal{N}_i} \frac{|e_{ij}|}{R_{ij}} (\bar{u}^{(j)} - \bar{u}^{(i)}) \right) + |e_{iq}| \bar{q}^{(i)} + \frac{|e_{iT}|}{R_i} (\bar{T}^{(i)} - \bar{u}^{(i)}) \quad (66b)$$

$$= \sum_{j \in \mathcal{N}_i} \left(-\frac{|e_{ij}|}{R_{ij}} \bar{u}^{(i)} + \frac{|e_{ij}|}{R_{ij}} \bar{u}^{(j)} \right) + \left(-\frac{|e_{iT}|}{R_i} \bar{u}^{(i)} \right) + \left(|e_{iq}| \bar{q}^{(i)} + \frac{|e_{iT}|}{R_i} \bar{T}^{(i)} \right) \quad (66c)$$

$$= \sum_{j \in \mathcal{N}_i \cup \{T_b\}} \left(\bar{B}_{ij}^{(i)} \bar{u}^{(i)} + \bar{B}_{ij}^{(j)} \bar{u}^{(j)} \right) + \bar{f}^{(i)} \quad (66d)$$

650 where in eq. (66b) $|e|$ denotes the length ($d = 2$) or area ($d = 3$) of a component boundary
651 e . The $\bar{A}^{(i)}$, $\bar{B}_{ij}^{(i)}$, and $\bar{B}_{ij}^{(j)}$ quantities are provided in eq. (12).

652 The lumped-mass representation for the four-component TPS is shown in Fig. ???. Let
653 v_i represent the area of the i -th element, $\overline{\rho c_p}_i$, the heat capacity evaluated using the average
654 temperature $\bar{u}^{(i)}$, and $1/R_{ij} = 1/R_i(\bar{u}^{(i)}) + 1/R_j(\bar{u}^{(j)})$ the equivalent thermal resistance
655 between elements i and j . Leveraging the formulas from eqs. (11) and (12), the LCM
656 matrices are given by,

$$\bar{\mathbf{A}} = \begin{bmatrix} \overline{\rho c_p}_1 v_1 & 0 & 0 & 0 \\ 0 & \overline{\rho c_p}_2 v_2 & 0 & 0 \\ 0 & 0 & \overline{\rho c_p}_3 v_3 & 0 \\ 0 & 0 & 0 & \overline{\rho c_p}_4 v_4 \end{bmatrix}, \quad (67a)$$

$$\bar{\mathbf{B}} = \begin{bmatrix} \frac{1}{R_{12}} + \frac{1}{R_{14}} & -\frac{1}{R_{12}} & 0 & -\frac{1}{R_{14}} \\ -\frac{1}{R_{12}} & \frac{1}{R_{12}} + \frac{1}{R_{24}} + \frac{1}{R_{23}} & -\frac{1}{R_{23}} & -\frac{1}{R_{24}} \\ 0 & -\frac{1}{R_{32}} & \frac{1}{R_{32}} + \frac{1}{R_{34}} & -\frac{1}{R_{34}} \\ -\frac{1}{R_{14}} & -\frac{1}{R_{24}} & -\frac{1}{R_{34}} & \frac{1}{R_{14}} + \frac{1}{R_{24}} + \frac{1}{R_{34}} \end{bmatrix}, \quad \bar{\mathbf{f}} = \begin{bmatrix} \bar{q}^{(1)} \\ \bar{q}^{(2)} \\ \bar{q}^{(3)} \\ 0 \end{bmatrix} \quad (67b)$$

657 References

- [1] Adam J. Amar, A. Brandon Oliver, Benjamin S. Kirk, Giovanni Salazar, and Justin Drob. Overview of the charring ablator response (char) code. In AIAA, editor, *AIAA Aviation Forum*, 2016.
- [2] Guy L. Bergel, Frank B. Beckwith, Gabel J. de Frias, Kevin M. Manktelow, Mark T. Merewether, Scott T. Miller, Krishen J. Parmar, Timothy S. Shelton, Jesse T. Thomas, Jeremy T. Trageser, Benjamin T. Treweek, Michael V. Veilleux, and Ellen B. Wagman. *Sierra/SolidMechanics 5.6 User's Manual*, 2022.
- [3] Ricky T. Q. Chen, Yulia Rubanova, Jesse Bettencourt, and David Duvenaud. Neural ordinary differential equations, 2019.

- [667] [4] Jonathan Clausen, Victor Brunini, Lincoln Collins, Robert C Knaus, Alec Kucala, Stephen Lin, Daniel Robert Moser, Malachi Phillips, Thomas Michael Ranseggnola, Samuel Ramirez Subia, et al. Sierra multimechanics module: Aria verification manual-version 5.22. Technical report, Sandia National Lab.(SNL-NM), Albuquerque, NM (United States), 2024.
- [672] [5] Gary Cohen and Sebastien Pernet. *Finite Element and Discontinuous Galerkin Methods for Transient Wave Equations*. Springer Dordrecht, Le Chesnay and Toulouse France, 2018.
- [675] [6] Jianhao Fang, Weifei Hu, Zhenyu Liu, Yuhao Zhou, Chao Wei, and Jianrong Tan. A reduced order finite element-informed surrogate model for approximating global high-fidelity simulations. *Structural and Multidisciplinary Optimization*, 67(12), 2024.
- [678] [7] Matthew Gasch, Keith Peterson, Mairead Stackpoole, Ethiraj Venkatapathy, Gregory Gonzales, and Kyle Hendrickson. Development of advanced ablative carbon phenolic tps for future nasa missions and commercial space. In *38th Annual Small Satellite Conference*, Logan, Utah, May 2024.
- [682] [8] Micah A. Howard and Ben F. Blackwell. A multi-dimensional finite element based solver for decomposing and non-decomposing thermal protection systems. In AIAA, editor, *AIAA Aviation Forum*, 2015.
- [685] [9] Frank P. Incropera, David P. DeWitt, Theodore L. Bergman, and Adrienne S. Lavine. *Fundamentals of Heat and Mass Transfer*. Wiley, Hoboken, NJ, 7th edition, 2011.
- [687] [10] R. J. Klock and Carlos Cesnik. Nonlinear thermal reduced-order modeling for hypersonic vehicles. *AIAA Journal*, 55(7), 2017.
- [689] [11] Arun Govind Neelan. Linear and non-linear reduced order model of scramjet. In *Advances in Multidisciplinary Design, Analysis and Optimization*, pages 111–118, Singapore, 2025.
- [692] [12] Alberto Padovan, Blaine Vollmer, Francesco Panerai, Marco Panesi, Kelly A. Stephani, and Daniel J. Bodony. An extended bformulation for ablating-surface boundary conditions. *International Journal of Heat and Mass Transfer*, 218:124770, 2024.
- [695] [13] Eric Parish and Karthik Duraisamy. Non-markovian closure models for large eddy simulations using the mori-zwanzig formalism. *Phys. Rev. Fluids*, 2:014604, Jan 2017.
- [697] [14] Eric Parish and Karthik Duraisamy. A unified framework for multiscale modeling using the mori-zwanzig formalism and the variational multiscale method. *ArXiv*, 12 2017.
- [699] [15] Eric Parish and Karthik Duraisamy. *Coarse-Graining Turbulence Using the Mori-Zwanzig Formalism*. Cambridge University Press, Cambridge, 2025.
- [701] [16] Carlos A. Vargas Venegas, Daning Huang, Patrick Blonigan, and John Tencer. Physics-infused reduced-order modeling for analysis of multi-layered hypersonic thermal protection systems. *ArXiv*, 2025.

- 704 [17] Yongyong Xian, Baisong Pan, and Luping Luo. A new model updating strategy with
705 physics-based and data-driven models. *Structural and Multidisciplinary Optimization*,
706 64(1), 2021.
- 707 [18] Yin Yu, John Harlim, Daning Huang, and Yan Li. Learning coarse-grained dynamics
708 on graph. *arXiv preprint arXiv:2405.09324*, 2024.